Potential Predictability in the NCEP/CPC Dynamical Seasonal Forecast System

Michael W. Phelps[1], Arun Kumar[2], and James J. O'Brien[1]

---

[1]The Center for Ocean-Atmospheric Prediction Studies
The Florida State University
Tallahassee, FL 32306-2840

[2]NOAA/NCEP/NWS/Climate Prediction Center
Camp Springs, MD 20746-4304

Winter Temperature and Precipitation Verification of the NCEP Operational Climate Model

David J. Salapata[1], Wayne Higgins[2], Jae-Kyung Schemm[2], and James J. O'Brien[1]

COAPS Technical Report
2002-04
August, 2002

FOREWORD

COAPS is an Applied Research Center funded by the Office of Global Programs, NOAA. One of the activities of COAPS is cooperating with NCEP and GFDL. To this goal, we funded 2 OGP/NOAA fellowships. In the summer of 2001, Mr. Michael Phelps and Mr. David Salapata worked at NCEP with Dr. Arun Kumar, Dr. Jae-Kyung Schemm, and Dr. Wayne Higgins. These scientists provided the scientific direction for these projects.

Unfortunately, the project indicates that the NCEP Dynamical Seasonal Forecast System has no useful skill for surface temperature and precipitation. However, it shows modest skill for some extratropical upper troposphere climate patterns.

James J. O'Brien
Robert P. Lawton Distinguished Professor
Meteorology and Oceanography

Potential Predictability in the NCEP/CPC Dynamical Seasonal Forecast System

Michael W. Phelps[1], Arun Kumar[2], and James J. O'Brien[1]

Signal-to-Noise Ratio
JFM: 2-month lead

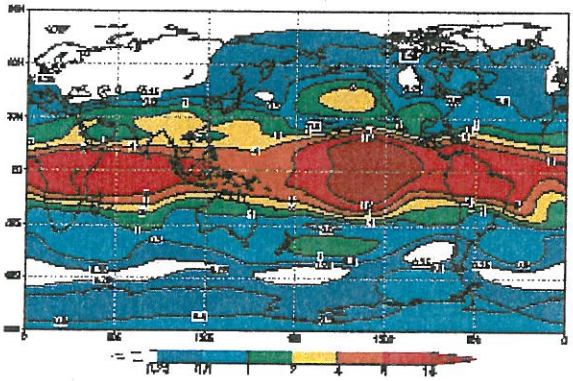

Anomaly Correlation
JFM: 2-month lead

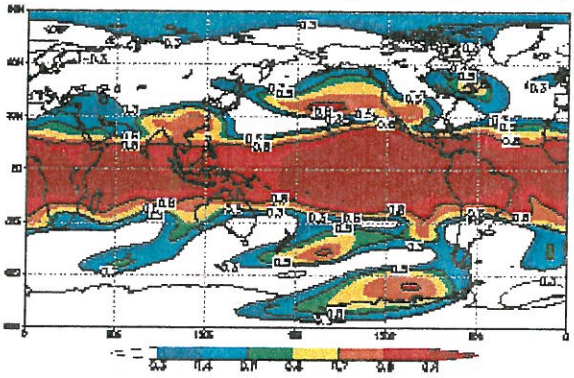

[1]Center for Ocean-Atmospheric Prediction Studies
The Florida State University
Tallahassee, FL 32306

in association with

[2]Climate Prediction Center
National Centers for Environmental Prediction
Camp Springs, MD 20746

COAPS Technical Report
2002-04a
August, 2002

1. INTRODUCTION

Predictability of atmospheric means on monthly or seasonal time scales has been historically viewed as a boundary forcing problem, with little attention paid to the possible effects of atmospheric initial conditions (IC). Such boundary forcings include sea surface temperature (SST), sea ice, snow cover, soil moisture, and other land surface conditions. It is the slow changes in these forcings, and the subsequent response to these changes, that are exploited in atmospheric general circulation model (AGCM) studies. Slowly varying anomalies in lower boundary forcing [i.e., sea surface temperature anomalies (SSTA)] can have a significant effect on the atmospheric response. This is the basis of potential predictability of monthly or seasonal means. (Brankovic et al. 1994).

Potential predictability (PP) of model simulated monthly or seasonal means can be determined by an analysis of the interannual variability of monthly or seasonal means (Chervin 1986). Atmospheric mean states are comprised of a naturally varying component and a boundary-forced component (Kumar et al. 1996). The naturally varying component is due to the internal dynamics of the atmosphere and is referred to as the internal variability (IV). The boundary-forced component is external to the atmosphere and is referred to as the external variability (EV). Under the assumption that internal variability is a measure of the unpredictable climate noise and the external variability is a measure of the potentially predictable signal, separation of the total variability into its internal and external components allows for the determination of a model's skill in

simulating the atmosphere by means of a signal-to-noise ratio (SNR). The potential for predictability can then be assessed by the amount to which the signal exceeds the noise (Shukla and Gutzler 1983).

One of the earliest studies of potential predictability was by Madden (1976). He estimated the so-called natural variability using time-averaged sea-level pressure analyses. This is analogous to IV and was referred to as "natural" since it would be present in an unchanging climate. Madden concluded that potential predictability is low because the total variability was not sufficiently larger than his estimates of natural variability. Shukla (1983) later pointed out that Madden's estimates of natural variability were too high, and as such the potential for predictability was underestimated. He noted that Madden's estimate of PP should be looked at as a lower bound for PP.

Kumar and Hoerling (1995) used the separation of total variability methodology on a nine-member ensemble of monthly mean 200-hPa eddy height anomalies for January from a model forced with monthly mean observed SSTs to evaluate the PP of atmospheric mean states. They found that large-scale atmospheric patterns associated with anomalous boundary forcings observed in El Niño/Southern Oscillation (ENSO) extreme events were produced at times in the extratropics. However, skill in the model simulations was not large away from the tropics, primarily due to large background climate noise. They concluded that the PP in the extratropics is low. Based on the idea that time-averaging has a similar effect as ensemble-averaging on the internal variance, they suggested that seasonal predictions should be improved over monthly predictions. Internal variance was found to decrease with increasing ensemble size, thus time averaging on longer time scales should produce a similar decrease in the internal variance

(Kumar and Hoerling 1995). This, in turn, would result in a higher SNR and a larger potential for predictability. They also noted that maxima in the boundary-forced signal coincided with two centers of the Pacific/North America (PNA) pattern and that this region would offer the best chance for predictability of wintertime climate patterns in the extratropics (Kumar and Hoerling 1998). Predictability was found to be larger in boreal winter because the strongest signal in model studies has consistently been found during Northern Hemisphere winter for both the tropics and extratropics. The wintertime signal has also been seen to increase with increasing strength of ENSO events, with a stronger response in warm events compared to cold events (Kumar and Hoerling 1997). The stronger response in the warm events may be due to a reduction in the wintertime signal during cold events (Hoerling et al. 1997).

The PNA pattern (Wallace and Gutzler 1981; Horel and Wallace 1981) is the most prominent teleconnection in Northern Hemisphere winter. This pattern has also been linked to tropical SST variability. A train of anomaly centers of opposite signs emanates from the tropical Pacific Ocean. In its positive phase, negative height anomalies are found over the North Pacific Ocean and Southeast United States, while positive anomalies are found over Hawaii and western Canada. The centers of action over the North Pacific and western Canada are generally the strongest (Horel and Wallace 1981) and it is these two centers that are associated with the maxima in boundary-forced signal noted above. Seasonal mean height anomalies are more likely to be in the positive PNA phase during El Niño, although the PNA pattern has been observed in non-El Niño years as well (Yarnal and Diaz 1986).

Reproduction of the PNA pattern in past model studies is not unprecedented. Blackmon et al. (1983) noted a PNA pattern in 200-hPa, 500-hPa, and 700-hPa geopotential height anomalies produced by an AGCM run in perpetual January mode with a representative SSTA in the tropical Pacific typical of warm ENSO events. Geisler et al. (1985) showed that the PNA pattern was a typical extratropical response in 200-hPa height anomalies for ENSO warm events of varying prescribed strengths. Lau (1985) also produced a PNA pattern similar to that seen in observations when forcing a model with observed SST in the tropical Pacific.

Recently, in the Applied Research Center at the Center for Ocean-Atmospheric Prediction Studies (COAPS), Salapata (2002) used output from the same model used in the present study to look at the relationship between various surface parameters and both the Arctic Oscillation (AO) and ENSO. He found that while the model performed well on the whole for seasonal averages, it had difficulty resolving the more extreme events in both precipitation and temperature. Capturing the observed effects of ENSO and AO was also found to be particularly problematic. Most troubling of all was the revelation that climatology was a better predictor of mean temperature and precipitation rate than the model over most of the United States. It was concluded that this model was not a useful forecasting tool for seasonal means of surface temperature and precipitation.

Apart from the well documented influence of SSTs on the interannual variability of the extratropical climate, other sources of predictability are continually being sought. One possible candidate is the low-frequency component of the atmospheric ICs, and their possible influence on the subsequent monthly and seasonal means (Shukla, 1983; Straus and Shukla, 2000). Conclusions about the impact of atmospheric ICs on monthly and

seasonal predictability, however, remain controversial. In this study, hindcasted 200-hPa geopotential heights from the second generation of the National Center for Environmental Prediction/Climate Prediction Center (NCEP/CPC) Dynamical Seasonal Forecast System starting from ICs with different lead times are examined to determine the role of atmospheric ICs in predicting monthly and seasonal mean atmospheric states. Skill of model simulations is determined by SNRs and anomaly correlations (AC) between ensemble-averaged height anomalies and NCEP/National Center for Atmospheric Research (NCAR) Reanalysis anomalies. If the atmospheric ICs have any positive influence, it is expected that simulations with a shorter lead time will provide a more skillful representation of the monthly and seasonal mean states of the upper atmosphere.

In section 2, a brief description of the NCEP Dynamical Seasonal Forecast System is presented and is followed by a description of the model and NCEP/NCAR Reanalysis data. Section 3 outlines the methods used to determine model biases, to separate the total variability into internal and external components, and to determine the level of skill obtained in the model hindcasts. Results are presented in section 4, with their discussion following in section 5.

2. DATA

a. Model

The coupled atmosphere-ocean general circulation model (GCM) used in this study is the second generation of NCEP's Dynamical Seasonal Forecast System. Implemented in April 2000, the second generation system was designed with a primary goal of refining predictions in the winter season. A brief description of some of the coupled model's components and characteristics are presented. A more detailed description can be in found in Kanamitsu et al. (2002b).

The AGCM dynamics incorporate the spectral method of Kanamitsu (1989). The atmosphere-only forecast model runs in T62L28 reduced grid resolution, providing an approximate 200 km resolution in the horizontal with 28 vertical layers. Model physics were taken from the operational medium range NCEP/Department of Energy (DOE) Reanalysis-II model with a few notable changes (Kanamitsu et al. 2002a). The convective parameterization scheme in this model is the Relaxed Arakawa-Schubert (RAS) scheme (Moorthi and Suarez 1992), as opposed to the Simplified Arakawa-Schubert (SAS) scheme (Pan and Wu 1995) used in the operational NCEP/DOE model. The RAS scheme was found to reproduce the PNA response much more accurately than the SAS scheme, especially for the PNA center over northern Canada. The original Reanalysis-II model was found to have a considerable warm bias, and significant testing

was done with various parameterization schemes to reduce this bias. Changes from the Reanalysis-II model that resulted in a reduction of the warm bias include the use of Chou's longwave radiation scheme (Chou and Suarez 1994), the original Slingo cloud scheme (Slingo 1987), and smoothed mean orography.

The land model in the AGCM is based on the Oregon State University land model (Pan and Mahrt 1987). The two soil-layer model provides soil temperature, soil water content, and canopy water content to the atmosphere and also includes simple snow physics. Vegetation and soil types used in the land model are derived from the Simple Biosphere Model climatology (Dorman and Sellers 1989).

The coupled dynamical seasonal prediction system at NCEP also includes prediction of SST based on a comprehensive coupled ocean-atmosphere GCM. The ocean GCM (OGCM) in this system is a modified version of the Geophysical Fluid Dynamics Laboratory (GFDL) tropical oceans model. The domain covers the Pacific Ocean basin from 45°S to 55°N and 120°E to 70°W. Resolution in the zonal direction is 1.5°, but meridional resolution is not uniform. In the equatorial region between 10°S and 10°N, the meridional resolution is 1/3°. The meridional resolution increases linearly from 1/3° to 1°, poleward from 10° to 20°. Outside of 20°, the meridional resolution is 1°. Vertically, there are 28 layers, 18 of which are in the top 400 m of the surface, with variable bottom topography. Vertical mixing is handled by a Richardson number-dependent scheme developed by Pacanowski and Philander (1981). A more detailed description of the OGCM is provided in Ji et al. (1995).

For production of the seasonal forecasts only, the OGCM is "one-way anomaly coupled" to a T42L18 AGCM, which is similar to the higher resolution model described

above but with an approximate horizontal resolution of only 300 km. Total SSTs from the OGCM are used to force the low resolution AGCM, while anomalies of momentum, heat, and fresh water fluxes from this lower resolution AGCM are added to climatological means to force the OGCM. A two-tiered approach is then used to drive the T62L18 atmospheric forecast model with the predicted SSTA obtained from the coupled ocean-atmosphere model. Over a period of one month, 16 runs are made from differing atmospheric initial conditions, resulting in a 16-member ensemble of SSTA. The predicted SSTAs from the first tier are available over the Pacific basin only. In the second tier of this approach, the ensemble-averaged SSTAs from tier one are blended with the observed SSTAs derived from the NCEP weekly SST analysis outside of the Pacific basin described above to comprise global SSTA fields. These anomalies outside of the tropical Pacific basin are damped to climatology with an e-folding time of 90 days. The anomalies are used as the lower boundary condition for the higher resolution atmosphere-only tier-2 forecast model.

The tier-2 seasonal atmospheric prediction system consists of two components. Each month, a set of hindcast runs initialized with observed atmospheric ICs and forced with observed SSTs for the period 1979-1999 is first done. An additional set of forecast runs forced with the predicted SSTAs is then made. The hindcast runs provide model climatologies from which the predicted anomalies are computed.

Real-time atmospheric analyses available in T62L28 resolution from the Reanalysis-II are used for atmospheric initial conditions. These analyses contain both high and low frequency modes of atmospheric variability, such as the PNA pattern, the North Atlantic and Arctic Oscillations, and individual synoptic systems. Land initial

conditions are taken from the Reanalysis-II climatology for soil wetness and snow cover. Climatological vegetation cover and types are used since these observations are not readily available over the period 1979-1999. Ocean initial conditions are derived from the GFDL real-time ocean data assimilation system. Weekly analyses of subsurface ocean temperature, SST, and sea surface height are used as initial conditions in the OGCM.

One other major component in the NCEP/CPC seasonal forecast system is the inclusion of hindcasts. Prior to the forecasts being made, 21 years of hindcasts are made for each of the six full months being forecast in that particular model run. Hindcasts are produced by the atmosphere-only model described above, which is initialized with past observed atmospheric conditions from 0000 UTC and 1200 UTC on the first five days of the initialization month for each of the 21 years. The only external boundary forcing is observed global monthly mean SSTs. Since SSTs are updated monthly, each simulation for a particular month, for example, January 1980, is subjected to identical lower boundary forcing, regardless of whether the starting month is September or December. Land initial conditions are the same as those described above for the forecast model to ensure that the hindcast climatology is as consistent with the forecast as possible (Kanamitsu et al. 2002b).

b. Model Data

The data used in this study are AGCM hindcasted 200-hPa geopotential heights for January, February, and March for the period 1980-2000 (Table 1). The use of

Table 1. Schematic representation of model output for this study. **BOLD** months represent the monthly data used and *italicized* months are the initialization months. (NOTE: JAN data from the July and August runs are not used, as explained in the text.)

JAN											
Jul	Aug	Sep	Oct	Nov	Dec	JAN					
	Aug	Sep	Oct	Nov	Dec	JAN	Feb				
		Sep	Oct	Nov	Dec	**JAN**	Feb	Mar			
			Oct	Nov	Dec	**JAN**	Feb	Mar	Apr		
				Nov	Dec	**JAN**	Feb	Mar	Apr	May	
					Dec	**JAN**	Feb	Mar	Apr	May	Jun

JFM											
		Sep	Oct	Nov	Dec	**JAN**	**FEB**	**MAR**			
			Oct	Nov	Dec	**JAN**	**FEB**	**MAR**	Apr		
				Nov	Dec	**JAN**	**FEB**	**MAR**	Apr	May	
					Dec	**JAN**	**FEB**	**MAR**	Apr	May	Jun

hindcasts initialized and forced with past observed atmospheric and oceanic conditions provides an estimation of the upper limit of a model's forecast skill, thereby justifying inferences made from hindcast results about monthly and seasonal forecasts. In accordance with past studies, the 200-hPa height anomaly fields are considered to be representative of the midlatitude response to the tropical Pacific SSTs (Geisler et al. 1985). For January (JAN) monthly means, integrations with lead times of July, August, September, October, November, and December are available. However, modifications in the model between the August and September initializations require that available data from the July and August runs be neglected for this study. The daily model fields at 2.5° x 2.5° latitude/longitude resolution are averaged to produce monthly mean JAN 200-hPa geopotential height fields. From the four available sets of hindcast runs, a total of 840 JAN simulations are made. For January/February/March (JFM) seasonal means, integrations with lead times of September, October, November, and December are used. The 3-month daily output is averaged to produce seasonal mean JFM 200-hPa geopotential height fields. For the JFM seasonal means, a total of 840 simulations are also available. For consistency between JAN and JFM means, the AGCM simulations from December ICs are referred to as the one month lead time, the simulations from November ICs are referred to as the two month lead time, the simulations from October ICs are referred to as the three month lead time, and the simulations from September ICs will be referred to as the four month lead time.

For each of the 21 years in a particular model run, an ensemble mean 200-hPa height field is calculated by averaging the 10 members in the ensemble. The mean of these 21 ensemble averages determines the model climatology (Fig. 1 for JAN, Fig. 2 for

JFM) for that particular simulation's lead time. Hindcast height anomalies (HA) are obtained by subtracting the 21-year climatology from each individual ensemble member.

c. Reanalysis Data

For comparisons to model data, monthly mean JAN and seasonal mean JFM 200-hPa geopotential heights for 1980-2000 are derived from the NCEP/NCAR 50-Year Reanalysis (Kistler et al. 2001). These data are readily available from the NOAA-Cooperative Institute for Research in Environmental Sciences (CIRES) Climate Diagnostics Center. The Reanalysis climatologies for JAN and JFM (Fig. 3) are computed by averaging the 21 years of JAN and JFM data, respectively. Height anomalies for the Reanalysis data are calculated in the same manner as described above for the model data.

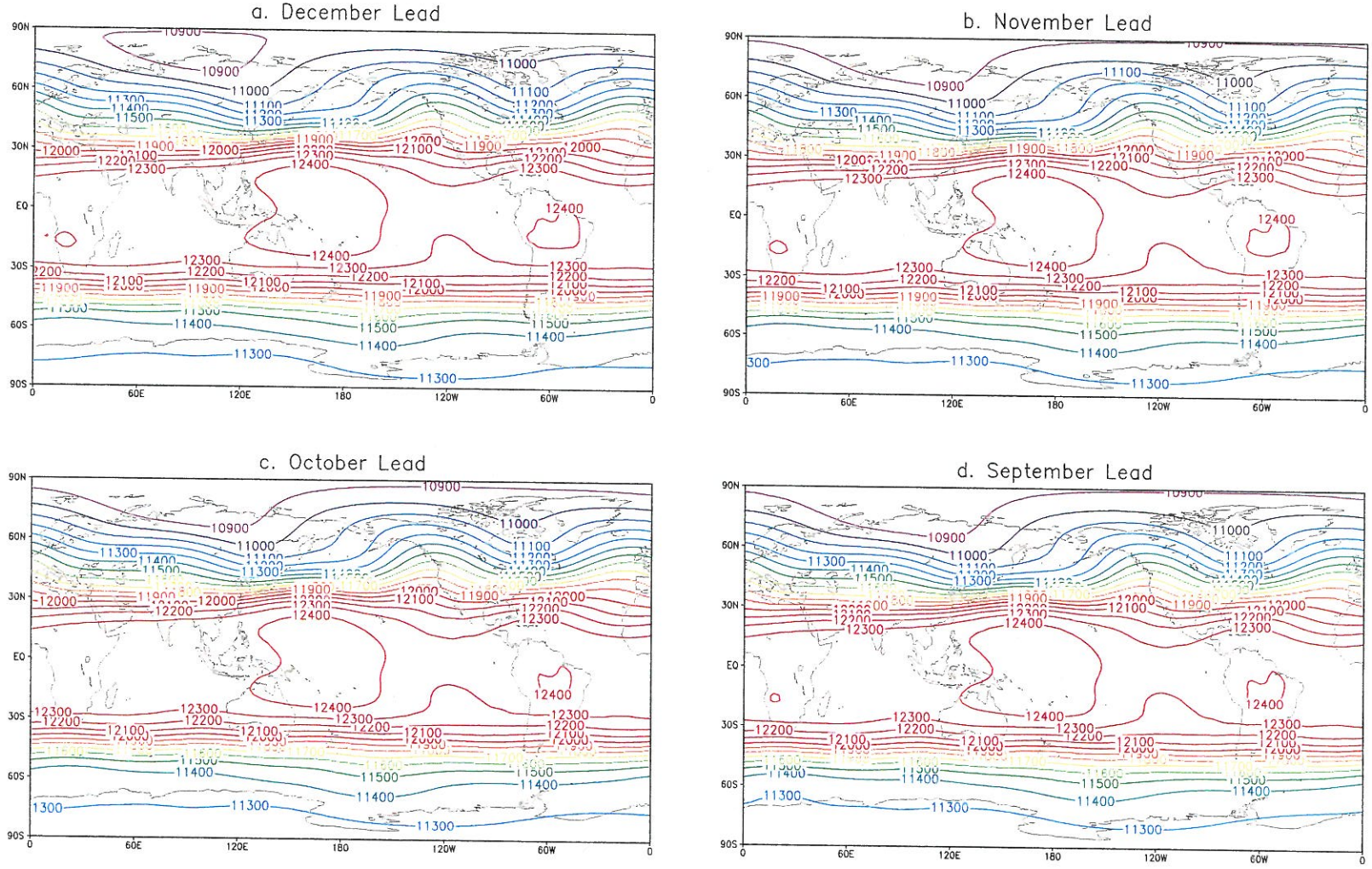

Figure 1. Monthly mean JAN model hindcast climatologies of 200 hPa geopotential heights (in m) from the NCEP Dynamical Seasonal Forecast System for the period 1980-2000 for the a) December initialization, b) November initialization, c) October initialization, and d) September initialization. Contour interval is 100 m.

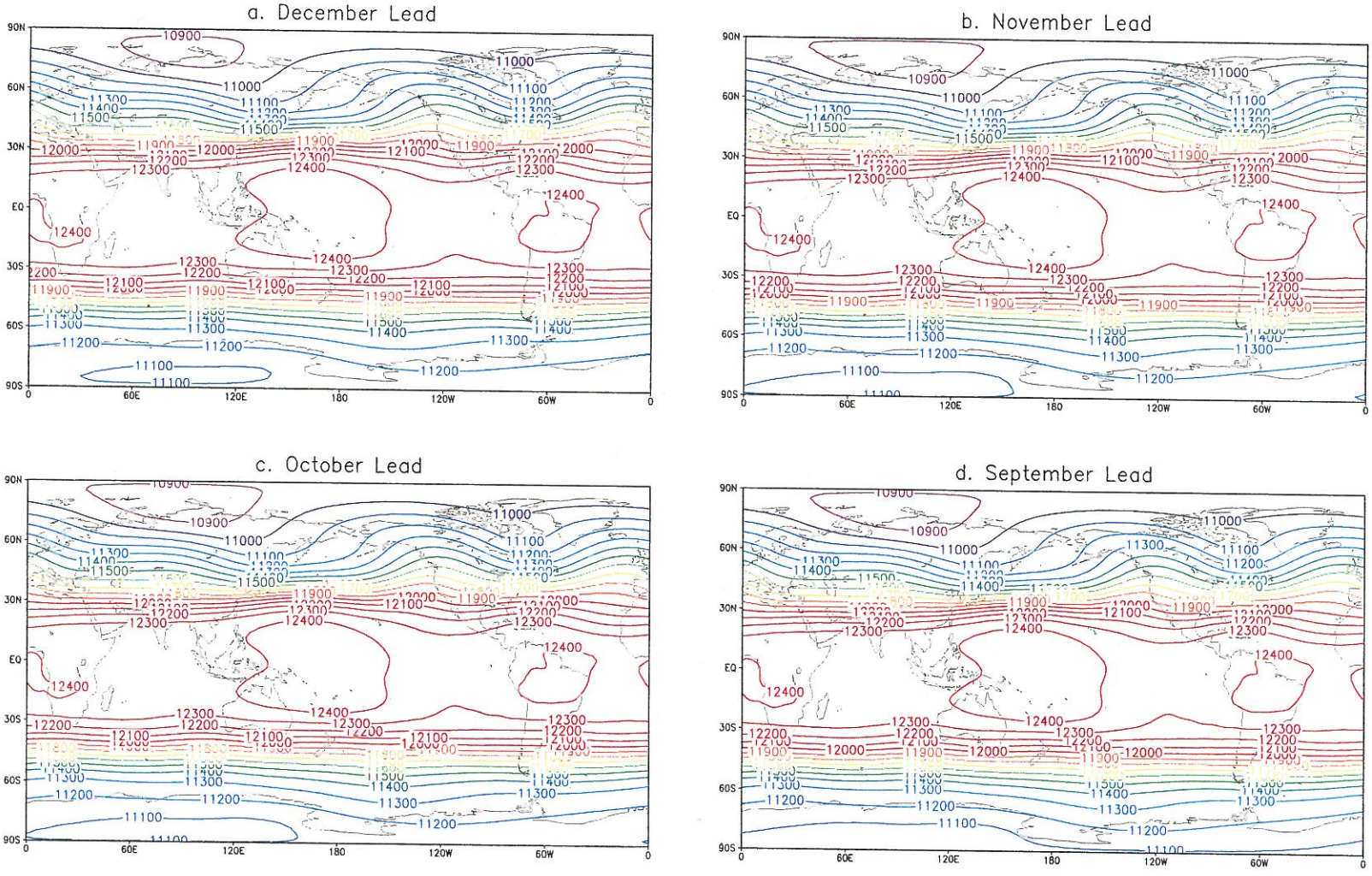

Figure 2. Seasonal mean JFM model hindcast climatologies of 200 hPa geopotential heights (in m) from the NCEP Dynamical Seasonal Forecast System for the period 1980-2000 for the a) December initialization, b) November initialization, c) October initialization, and d) September initialization. Contour interval is 100 m.

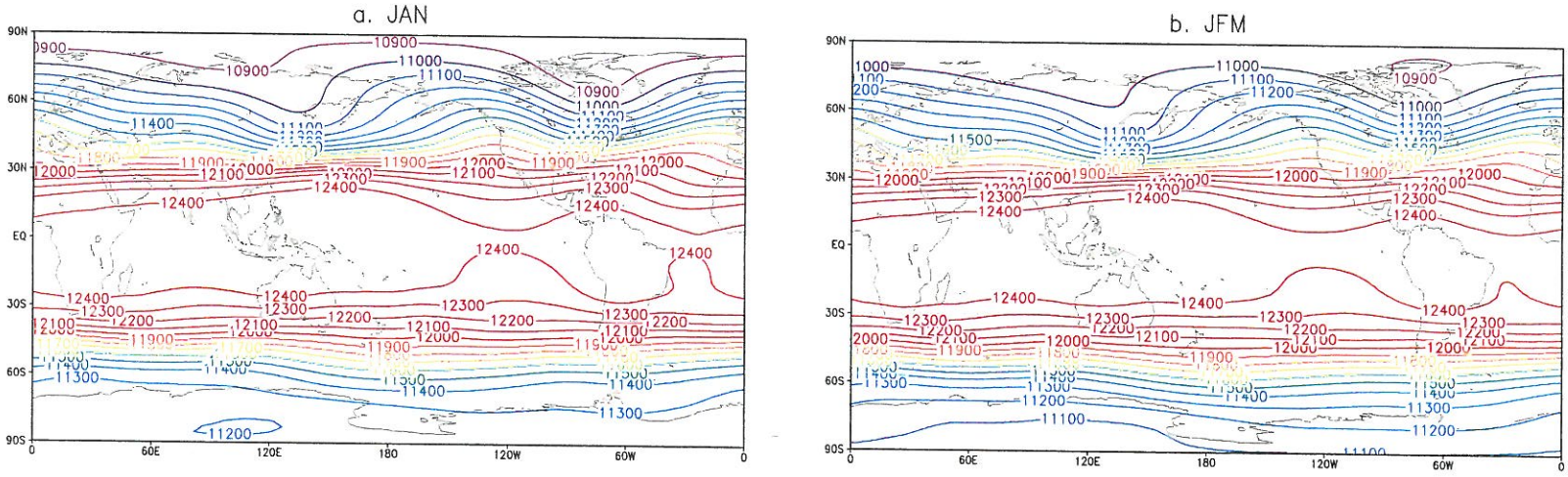

Figure 3. Climatologies of 200 hPa geopotential heights (in m) for a) monthly mean JAN and b) seasonal mean JFM from the NCEP/NCAR Reanalysis for the period 1980-2000. Contour interval is 100 m.

3. ANALYSIS PROCEDURES

Model biases for each lead time are formed by subtracting the appropriate Reanalysis climatology from the various model climatologies. Model climatologies are computed by averaging all 210 simulations (10-member ensemble for 21 years) for a given lead time. Reanalysis climatologies for JAN and JFM are calculated by averaging the 21 monthly mean or seasonal mean fields derived from the NCEP/NCAR Reanalysis project for the period 1980-2000.

Analyses of variance of model HA are performed in order to assess the potential predictability of monthly and seasonal atmospheric conditions by isolating the potentially predictable signal produced by the external boundary forcing from the unpredictable background climate noise. Let $A_{h\alpha i}$ represent a hindcast HA, where the subscript α denotes a particular year with unique SST state and the subscript i denotes a particular member within an ensemble. Then, the ensemble-averaged anomaly for unique SST state is defined as

$$\overline{A_{h\alpha}} = \frac{1}{10} \sum_{i=1}^{10} A_{h\alpha i} \quad . \tag{1}$$

Despite the fact that each member in an ensemble is subjected to the same SST forcing, the atmospheric anomalies are a blend of the response due to anomalous SSTs and atmospheric internal variability. It is the ensemble average that represents the atmospheric response (Kumar and Hoerling, 1995) and is the most likely outcome for the

observed anomalies. The variability among the 10 ensemble members in a particular year is termed the internal variability (IV) and is given by

$$\sigma_{\alpha}^{2}=\frac{1}{10}\sum_{i=1}^{10}(A_{h\alpha i}-\overline{A_{h\alpha}})^{2} \quad . \tag{2}$$

The IV can differ from year to year due to differences in SST states used to force the model. The mean internal variability (MIV) across all SST states, then, is the average of the IV over the entire 21-year period and is defined as

$$\sigma_{I}^{2}=\frac{1}{21}\sum_{\alpha=1}^{21}\sigma_{\alpha}^{2} \quad . \tag{3}$$

This MIV is a measure of the background climate noise, which is not predictable from the knowledge of SSTs.

The external variance (EV) is spread among ensemble-averaged anomalies and represents the variance due to interannual changes in SST. It is defined as

$$\sigma_{E}^{2}=\frac{1}{21}\sum_{\alpha=1}^{21}(\overline{A_{h\alpha}}-\overline{A_{h}})^{2} \quad , \tag{4}$$

where $\overline{A_{h}}$ is the mean anomaly of the entire population and is, necessarily, zero. The EV is a measure of the boundary-forced signal, which is potentially predictable. The total variance is the sum of the mean internal and external variances, such that

$$\sigma_{T}^{2}=\sigma_{I}^{2}+\sigma_{E}^{2} \quad . \tag{5}$$

A signal-to-noise ratio (SNR) can be defined as the ratio of external variance to mean internal variance and is given by

$$SNR=\frac{\sigma_{E}^{2}}{\sigma_{I}^{2}} \quad . \tag{6}$$

Correlations in time between ensemble-averaged hindcast anomalies $(\overline{A_{h\alpha}})$ and Reanalysis anomalies $(A_{r\alpha})$ for each grid point are calculated using

$$AC = \frac{\sum_{\alpha=1}^{21} (\overline{A_{h\alpha}} A_{r\alpha})}{(\sum_{\alpha=1}^{21} \overline{A_{h\alpha}}^{2})^{1/2} (\sum_{\alpha=1}^{21} A_{r\alpha}^{2})^{1/2}} , \qquad (7)$$

in an effort to determine areas where the model skillfully hindcasted the climate anomalies. This is done for the period 1980-2000 and also for subsets of ENSO warm and cold events and ENSO neutral events. Both extremes of ENSO are treated as a whole because of the small number of warm and cold events in this period. An anomaly correlation of 0.5 or greater implies useful skill in the model hindcasts (Kumar et al. 1996). In addition, correlations greater than 0.3 are assumed to show some skill, while correlations in excess of 0.8 exhibit significant skill.

Classification of ENSO events is provided by NCEP/CPC and is summarized for 1980-2000 in Table 2. The process is subjective, as a group of CPC scientists have individually categorized each season since 1950 based on the pattern and magnitude of SST in the tropical Pacific along the Equator from the International Dateline to 150°W. The classification, then, is the consensus of individual evaluations. For this study, the strong (W+) and moderate (W) warm events from the NCEP/CPC classification are considered as the "warm" events, the weak warm (W-), neutral (N), and weak cold (C-) events are considered as the "neutral" events, and the moderate (C) and strong (C+) cold events are considered as the "cold" events. Since ENSO events begin in the summer of a classified year, the classification for JAN and JFM appears to lag by one year. For

Table 2. Classification of ENSO Events for JAN and JFM for the period 1980-2000. "Warm" denotes the strong and moderate warm events from the NCEP/CPC classification, "Neutral" denotes the weak warm, neutral, and weak cold events, and "Cold" denotes the moderate and strong cold events.

Warm	Neutral	Cold
1983 W+	1980 W-	1989 C+
1987 W	1981 N	1999 C
1992 W+	1982 N	2000 C+
1998 W+	1984 C-	
	1985 C-	
	1986 N	
	1988 W-	
	1990 N	
	1991 W-	
	1993 W-	
	1994 N	
	1995 W-	
	1996 C-	
	1997 N	

example, the extraordinary 1982-83 warm event shows up as 1983 for JAN and JFM, even though it began in the latter part of 1982. For the period 1980-2000, there are a total of four warm events, three cold events, and 14 neutral events.

Based on the above ENSO classification, composite ENSO warm and cold events can be formed for both the hindcast and Reanalysis data. Compositing extracts the common features in the atmospheric responses to different SST forcings (Kumar and Hoerling 1997). A total of 40 AGCM simulations comprise the hindcast warm composite and a total of 30 AGCM simulations make up the hindcast cold composite for each lead time. These AGCM composites are compared to the Reanalysis warm and cold composites, respectively. Comparisons are done for the PNA region bounded by 20°N, 70°N, 180°, and 60°W, a region where model simulations in the past have shown to be most skillful.

4. RESULTS

a. Analysis for JAN Means

The dominant feature in the JAN model biases (Fig. 4) for each lead time is a relatively strong negative bias spanning much of the South Pacific Ocean between 30°S and 60°S. Climatological model heights are more than 180 m less than Reanalysis heights just southeast of Australia. This negative bias extends over much of the globe, including Europe, Asia, Africa, and most of the Americas, while a positive bias is found over most of Antarctica. The bias pattern over the western portion of the Northern Hemisphere is reminiscent of the PNA pattern. The primary negative center just south of Alaska aligns well with the corresponding center of the PNA, while the positions of the secondary positive center north of the Hudson Bay and the tertiary negative center over the North Atlantic are shifted eastward in relation to the PNA. There appears to be a positive shift in the bias over the entire globe from the two-month lead to the one-month lead. The bias is consistent for the four-month, three-month, and two-month leads. In the December initialization, however, the negative centers in the South Pacific and south of Alaska are weaker while the positive center north of the Hudson Bay is stronger, with all differences on the order of 30 m. Such an effect can also be seen in northern Asia.

Analysis of variance techniques described above are used to separate the total variability into internal and external components to determine signal-to-noise ratios.

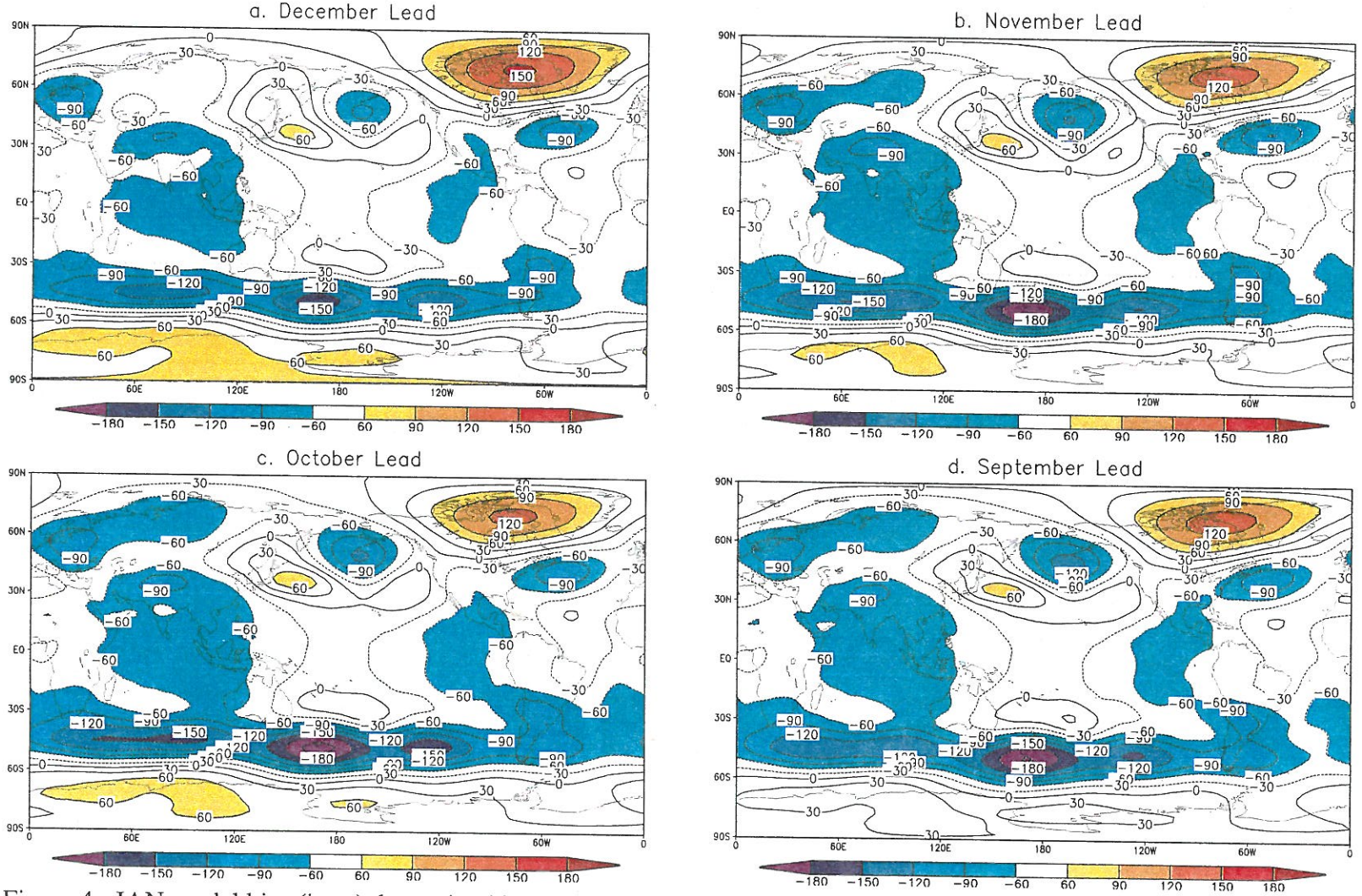

Figure 4. JAN model bias (in m) determined by subtracting the Reanalysis climatology from the model climatology for the a) December initialization, b) November initialization, c) October initialization, and d) September initialization. Contour interval is 30 m, with values greater than 60 m shaded yellow and red and values less than -60 m shaded blue and purple.

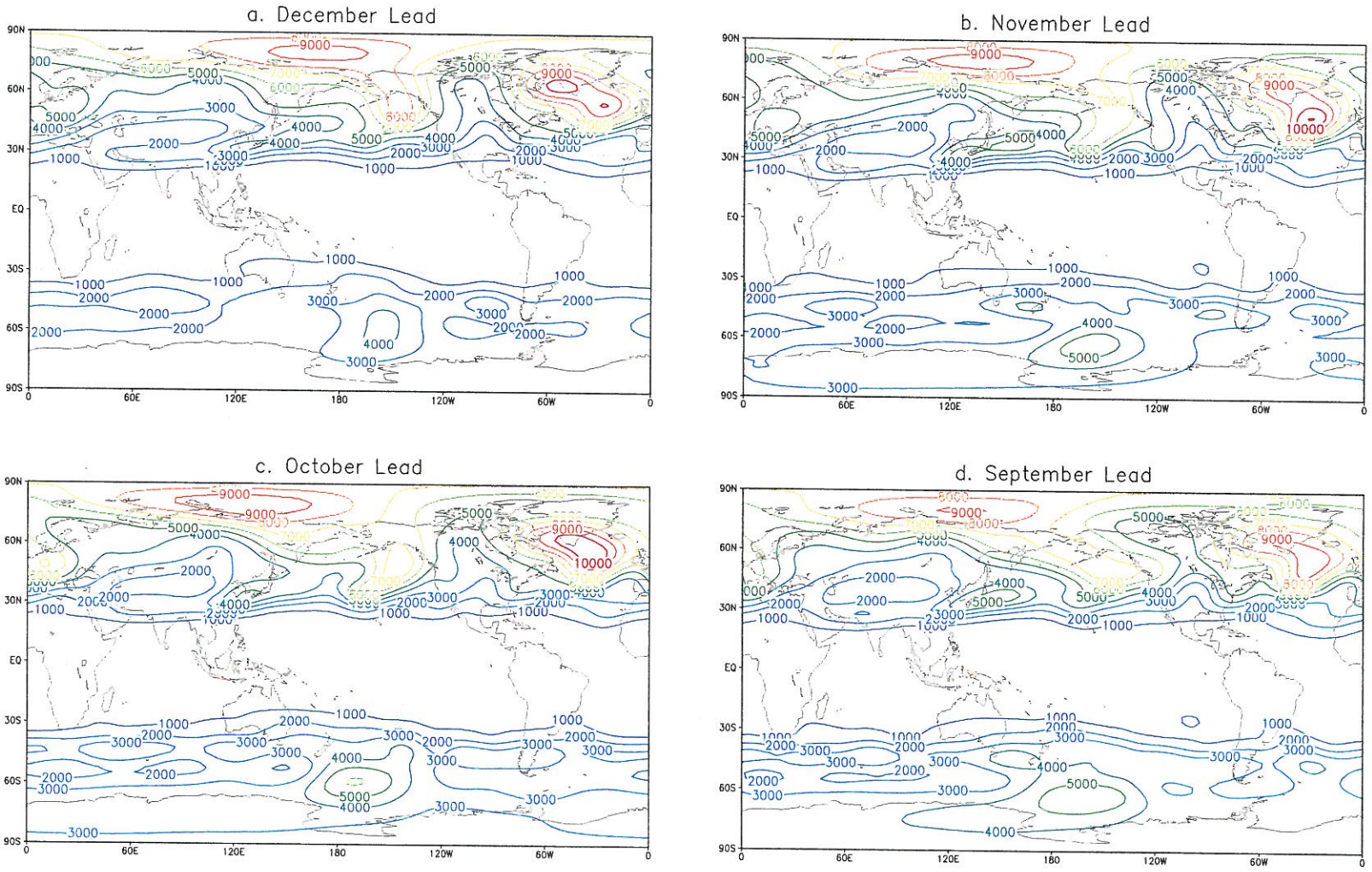

Figure 5. JAN mean internal variance (in m^2) for the a) December initialization, b) November initialization, c) October initialization, and d) September initialization. This shows the 21-year average of the variability among the 10 ensemble members in each year. Contour interval is 1000 m^2.

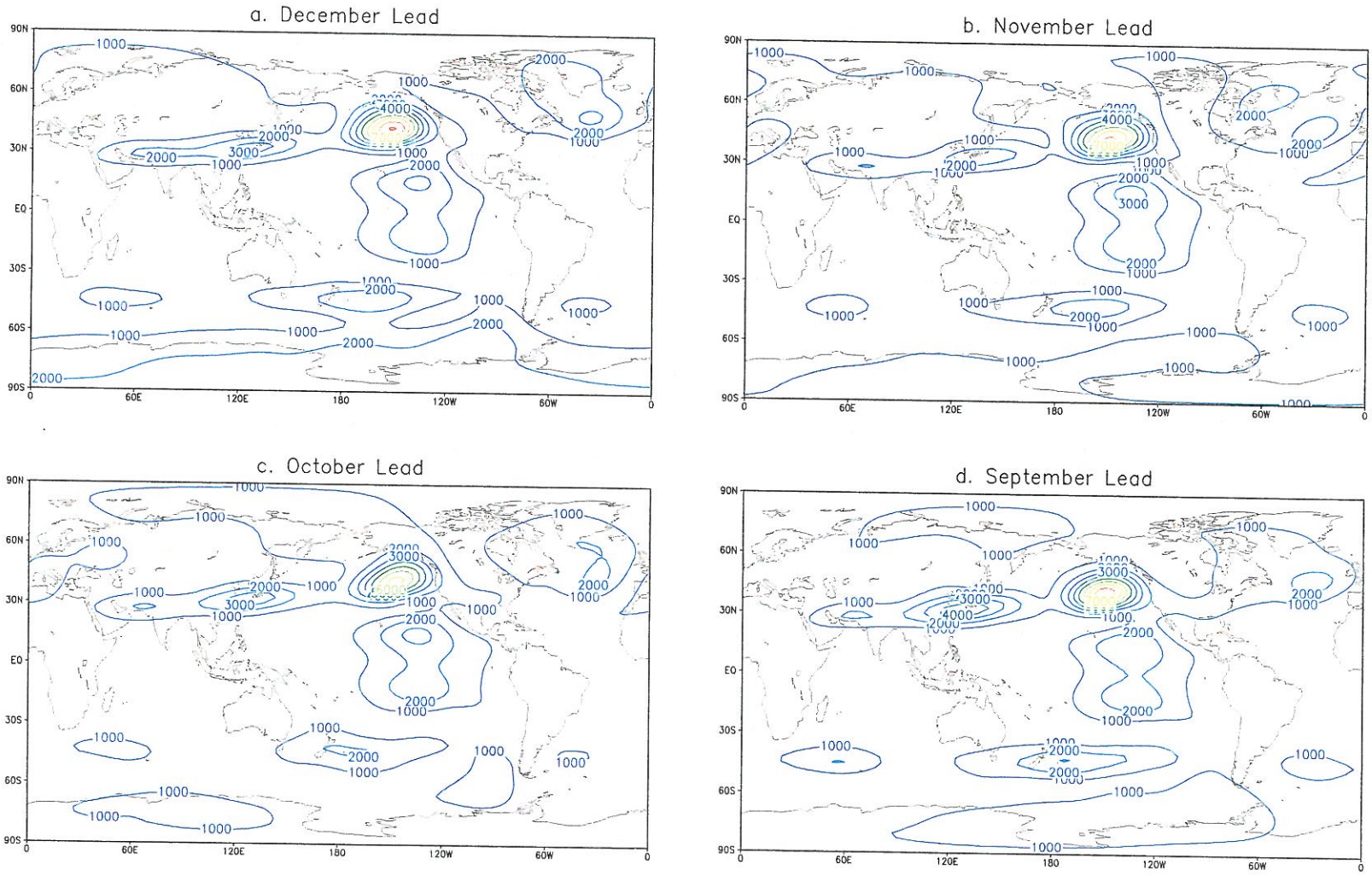

Figure 6. JAN external variance (in m^2) for the a) December initialization, b) November initialization, c) October initialization, and d) September initialization. This shows the variability among the ensemble-averaged anomalies over 21 years due only to interannual changes in SST. Contour interval is 1000 m^2.

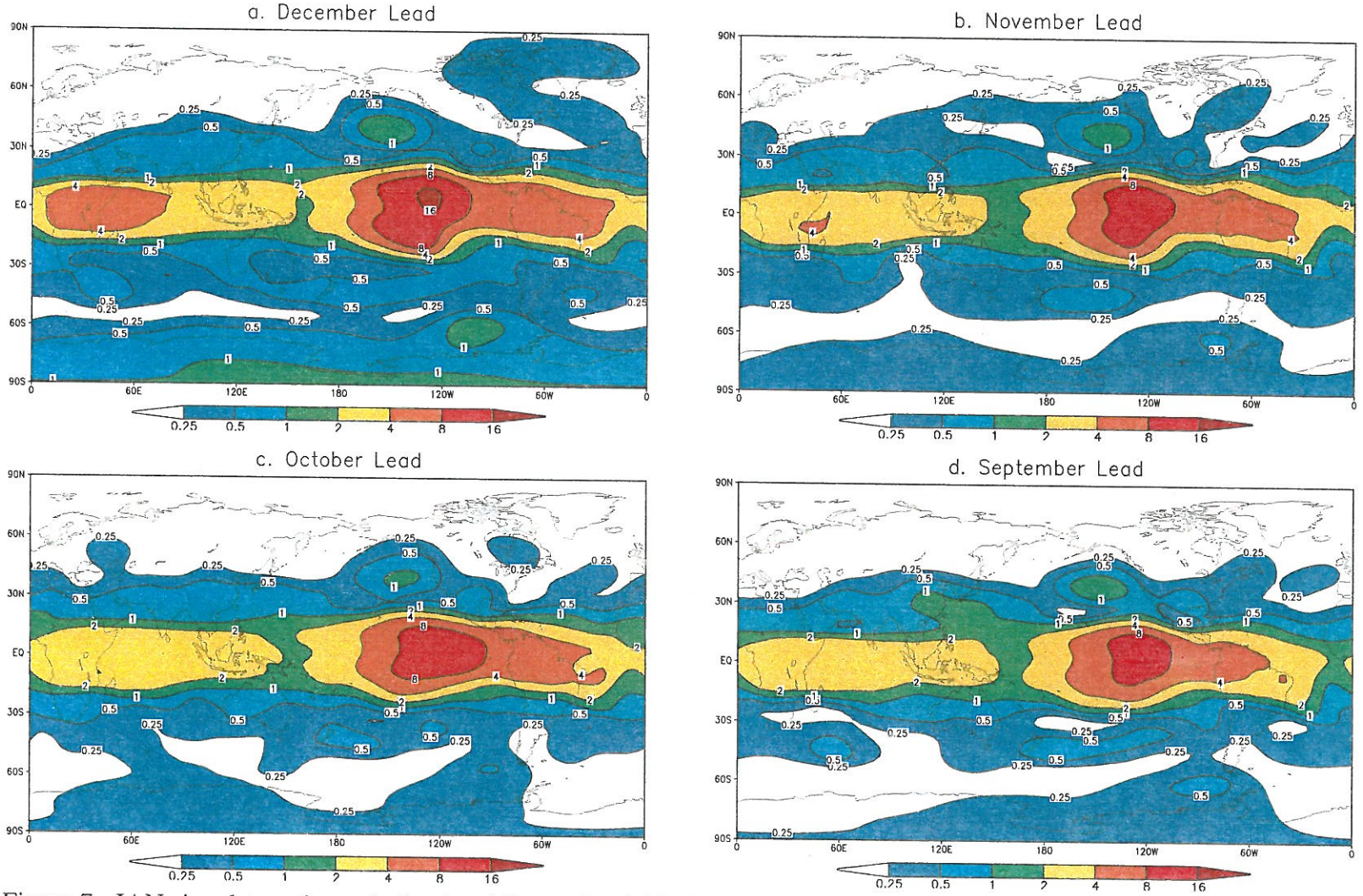

Figure 7. JAN signal-to-noise ratio for the a) December initialization, b) November initialization, c) October initialization, and d) September initialization. This is the ratio of external variance to mean internal variance. Contours for 0.25, 0.5, 1, 2, 4, 8, and 16 are shown.

Internal variability (Fig. 5) in the Northern Hemisphere extratropics is found to be about twice that in the Southern Hemisphere. Within 25-30° of the Equator, MIV is very small. Maximum MIV in the Northern Hemisphere is found over the North Atlantic and the Arctic Ocean and just north of the Ross Sea in the Southern Hemisphere. The pattern for MIV is fairly consistent regardless of lead time indicating little influence of atmospheric ICs.

Maps of EV (Fig. 6) show four main features: a) a dual-lobe pattern in the eastern tropical Pacific straddling the Equator, b) a local maximum in the South Pacific in the same area as the strongest negative bias, c) a slightly stronger local maximum centered just off the coast of China, and d) the dominant maximum in the North Pacific just south of Alaska, corresponding to one of the centers of action in the PNA pattern. These four features are consistent with each lead time, though there is a marked increase in EV over Antarctica for the one-month lead (Fig. 6a).

Signal-to-noise ratios (Fig. 7) are strongest over the eastern tropical Pacific, corresponding to one of the local maxima in EV described above. Areas where signal exceeds noise are generally contained in the tropics (within ~20° of the Equator) and span the entire tropical belt. In the extratropics, the lone area where SNR>1 for all lead times is in the North Pacific just south of Alaska, in the same area of the dominant maximum in EV. An interesting feature is the appearance of SNR>1 over Antarctica for the one-month lead (Fig. 7a), most likely the result of the noted increase in EV in the same area. The areal coverage of SNR>0.25 tends to increase as the lead time decreases. No such increase is observed in the total area where the signal exceeds the noise. Noticeable increases in SNR over the eastern tropical Pacific and equatorial Africa and the western

Indian Ocean can be seen as the lead time decreases. However, such details when SNR are this high to begin with are of little value or use.

Anomaly correlations for all 21 years (Fig. 8) show that the highest correlations between ensemble-averaged model-simulated JAN height anomalies and Reanalysis height anomalies are found in the tropical belt consistent with high SNR. The maximum AC, exceeding 0.9, is found in the tropical eastern Pacific. Local maxima in AC also correspond to the other three features described earlier in regard to EV. AC>0.5 are found in the South Pacific and off the coast of China. In the extratropics, the dominant feature is the AC center south of Alaska in the same region as the maximum EV. The strongest extratropical correlations are consistently found here. A new feature is the appearance of AC>0.5 in the Southern Ocean between 180° and 60°W for the four- and one-month leads. Correlations are not as strong in the October and November runs, but the pattern of increased AC in this area is persistent. Over the entire globe, AC is consistently the same, regardless of lead time.

Computing the AC for the seven ENSO warm and cold years (Fig. 9) shows that correlations are generally larger for the entire globe when compared to AC for 1980-2000. Areas of AC>0.9 are much larger and now found in the area of maximum EV just south of Alaska and off the coast of China. Correlations over the Southern Ocean now exceed 0.8 and are much more expansive. Also, significant AC greater than 0.8 are now found over portions of North America and the north Atlantic that were not present when all 21 years were considered as a whole.

For ENSO neutral years (Fig. 10), there is a sharp decrease in AC compared to ENSO warm and cold years over the entire globe, most noticeably in the vicinity of the

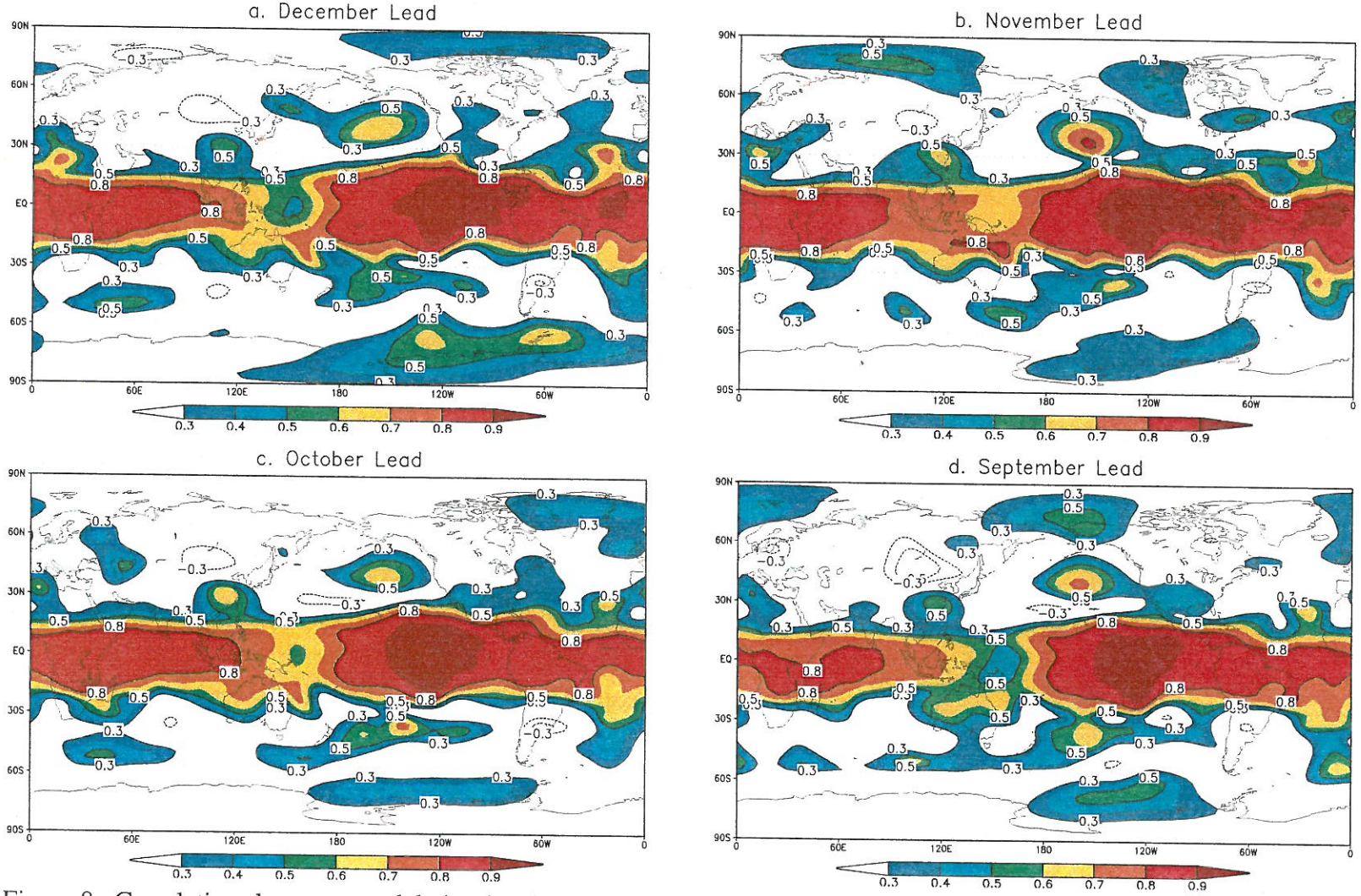

Figure 8. Correlations between model-simulated ensemble-averaged height anomalies and Reanalysis anomalies at 200 hPa for monthly mean JAN for a) December initialization, b) November initialization, c) October initialization, and d) September initialization. Contour interval is 0.1 for absolute values greater than 0.3. Positive (negative) contours are solid (dashed).

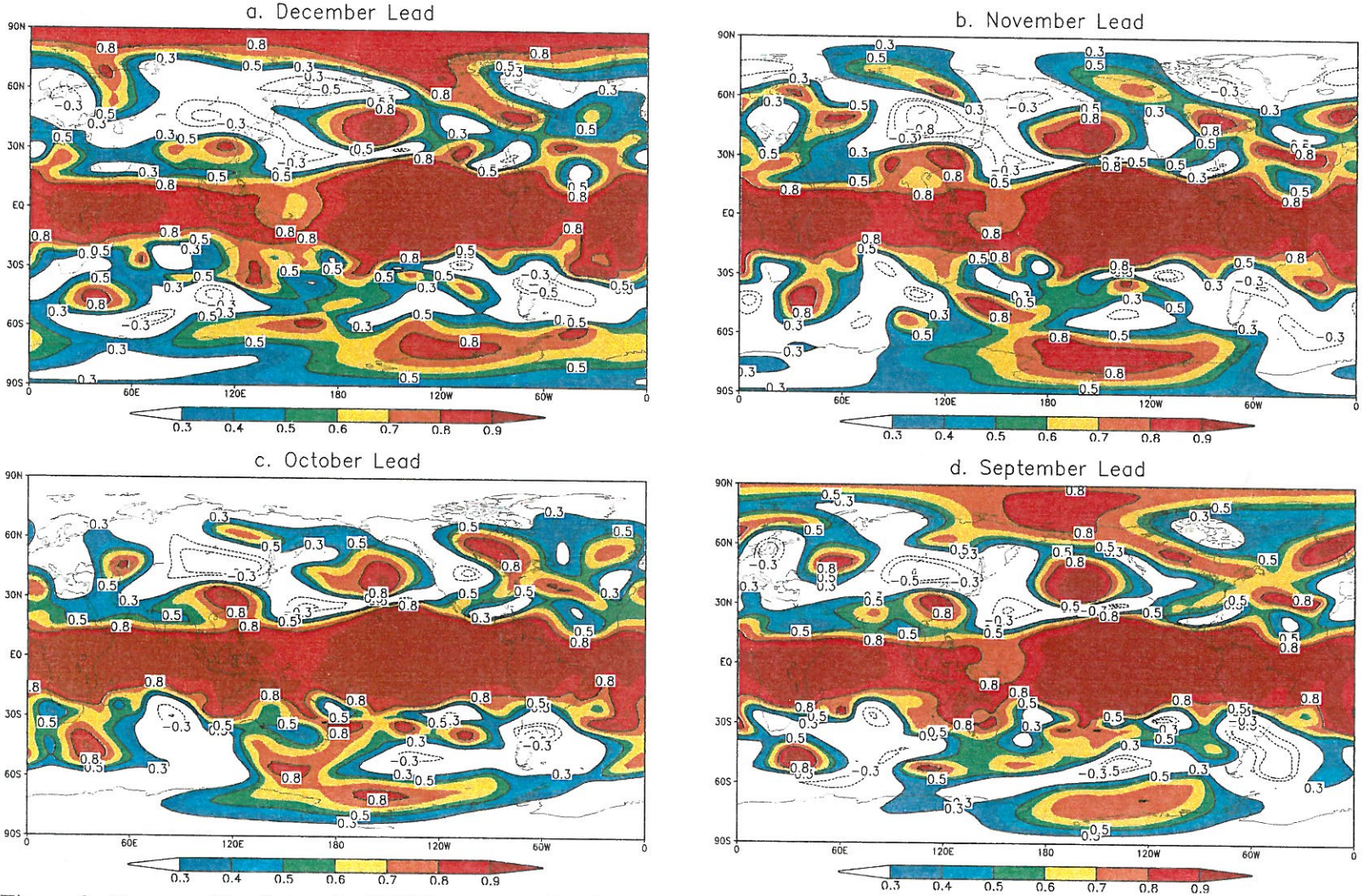

Figure 9. Same as Fig. 8, but for ENSO warm and cold events according to Table 2.

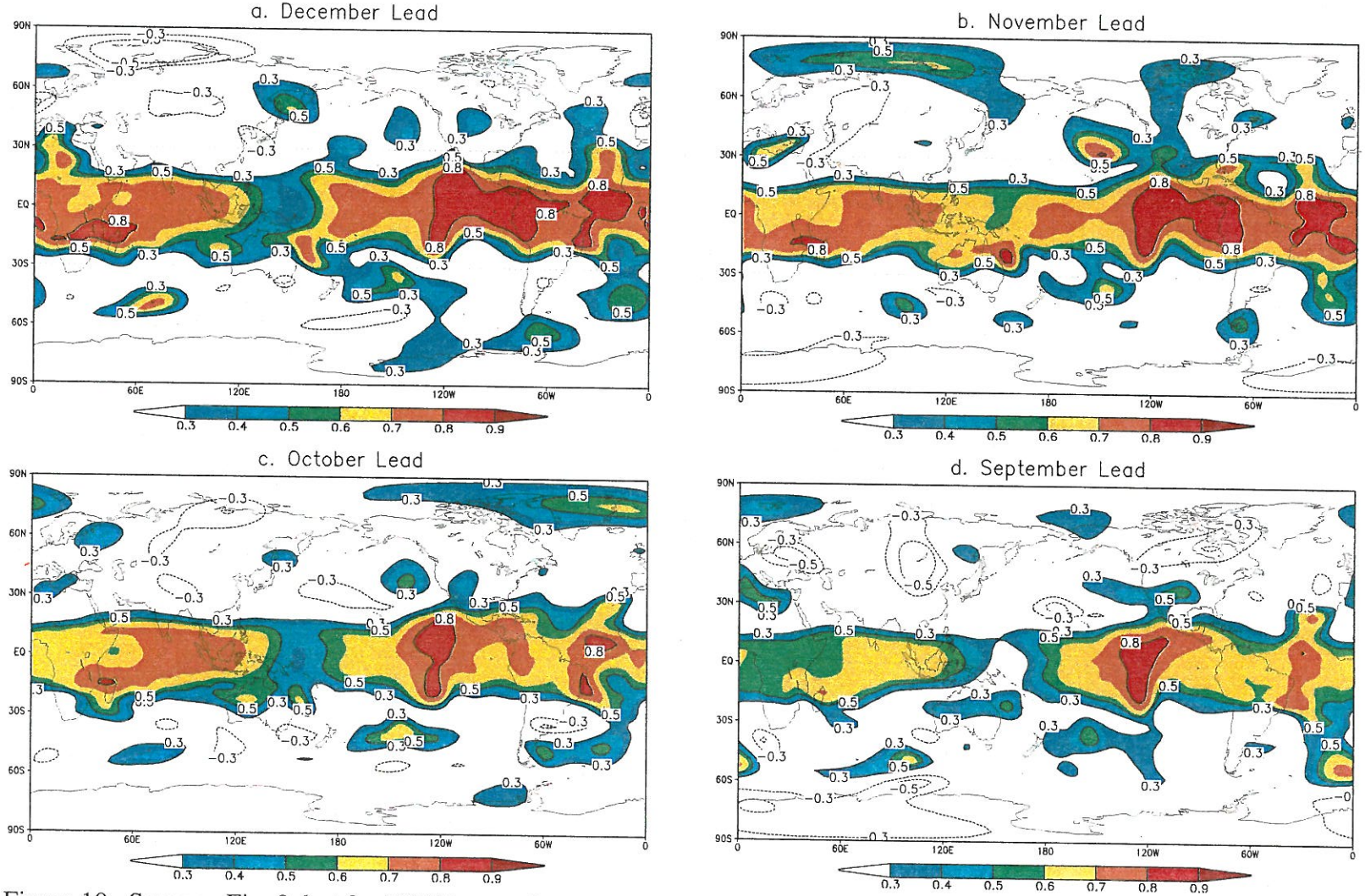

Figure 10. Same as Fig. 8, but for ENSO neutral events according to Table 2.

PNA center south of Alaska. The only area with AC>0.8 for neutral years is in the eastern tropical Pacific. Very little skill is exhibited in the Southern Ocean or off the coast of China. More skill is noted in the South Pacific, but not nearly as much as in ENSO warm and cold years.

To assess the model's ability to simulate ENSO events, composite warm and cold events were formed. In the warm composites (Fig. 11), Reanalysis data (Fig. 11a) show a strong negative anomaly center in the North Pacific in the same area as the maximum EV. The area of negative anomalies extends eastward over the southern United States and northern Mexico with a weak secondary negative center along the US/Mexico border. A strong positive anomaly is centered near Hudson Bay. Model composites (Figs. 11b, 11d, 11f, and 11h) show that a strong negative center of the same magnitude as that found in the Reanalysis composite is displaced slightly eastward. No secondary negative center is found in the model simulations, but the extension of the major center is approximately twice as strong as the Reanalysis. The positive center is not replicated as well in the model. The model composite anomaly is close in proximity to the Reanalysis composite, but its magnitude is less than half that found in the Reanalysis. Differences between the model composite and the Reanalysis composite (Figs. 11c, 11e, 11g, and 11i) show very little change as lead time decreases.

The pattern in the ENSO cold composite (Fig. 12) shows a response that is somewhat opposite in nature to the warm composite. In the Reanalysis composite (Fig. 12a), a positive anomaly center is now found south of Alaska in the northern Pacific. A negative anomaly is centered over northern Alaska, to the west of the warm composite's positive anomaly location over Hudson Bay. A distinct secondary positive anomaly is

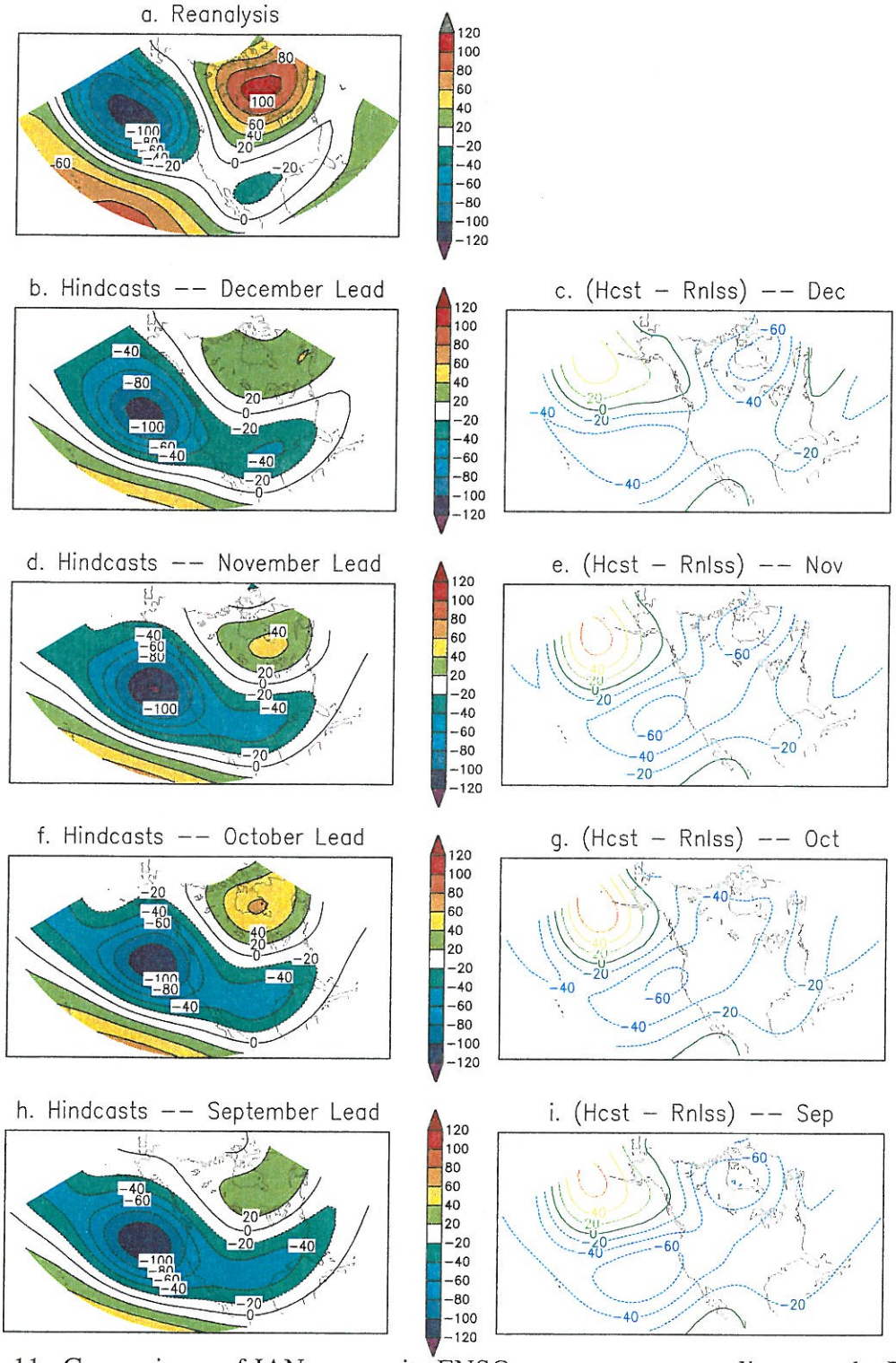

Figure 11. Comparisons of JAN composite ENSO warm event anomalies over the PNA region: a) Reanalysis, b) December initialization, c) difference (b-a), d) November initialization, e) difference (d-a), f) October initialization, g) difference (f-a), h) September initialization, and i) difference (h-a). Contour interval is 20 m.

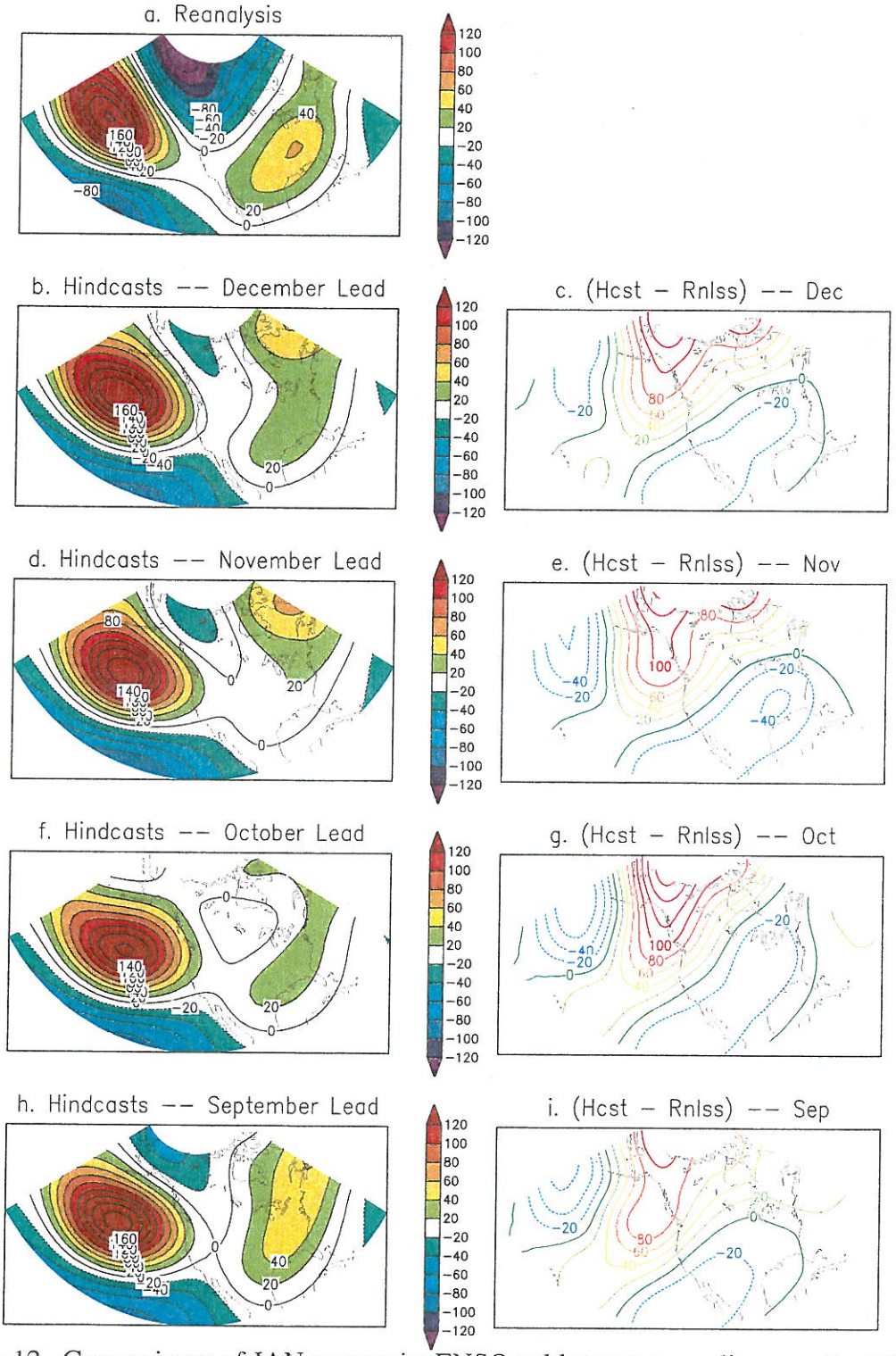

Figure 12. Comparisons of JAN composite ENSO cold event anomalies over the PNA region: a) Reanalysis, b) December initialization, c) difference (b-a), d) November initialization, e) difference (d-a), f) October initialization, g) difference (f-a), h) September initialization, and i) difference (h-a). Contour interval is 20 m.

located over the Mississippi Valley and covers much of the continental US. All three centers in the cold composite are more extreme than their warm composite counterparts. The model cold composites (Figs. 12b, 12d, 12f, and 12h) are not as consistent with different lead times compared to the warm years. However, the North Pacific center is still displaced slightly eastward as opposed to the Reanalysis. The negative center over Alaska is nearly non-existent in the model composites and the positive anomalies over the US are not as strong as the Reanalysis. Again, there is very little change in the difference maps (Figs. 12c, 12e, 12g, and 12i) with decreasing lead time.

b. Analysis for JFM Means

Model biases for JFM (Fig 13) are quite similar to those for JAN. There is a negative bias covering much of Europe, Asia, Africa, and the Indian Ocean and a PNA-like pattern over the western part of the Northern Hemisphere for each lead time. As expected, biases for JFM are more consistent for different lead times than are the biases for JAN. The magnitudes of the negative biases over the South Pacific and North Atlantic and the positive bias over Hudson Bay remain approximately the same as lead time shrinks from four months to one month. The only noticeable change is the reduction of the negative bias just south of Alaska. Also absent from the JFM biases is the positive bias over Antarctica.

Because JFM data are three-month seasonal averages, IV (Fig. 14) is reduced by about one-third. This is especially evident in the Northern Hemisphere. Reduction in the Southern Hemisphere is not quite as drastic, however, and the IV in the Northern

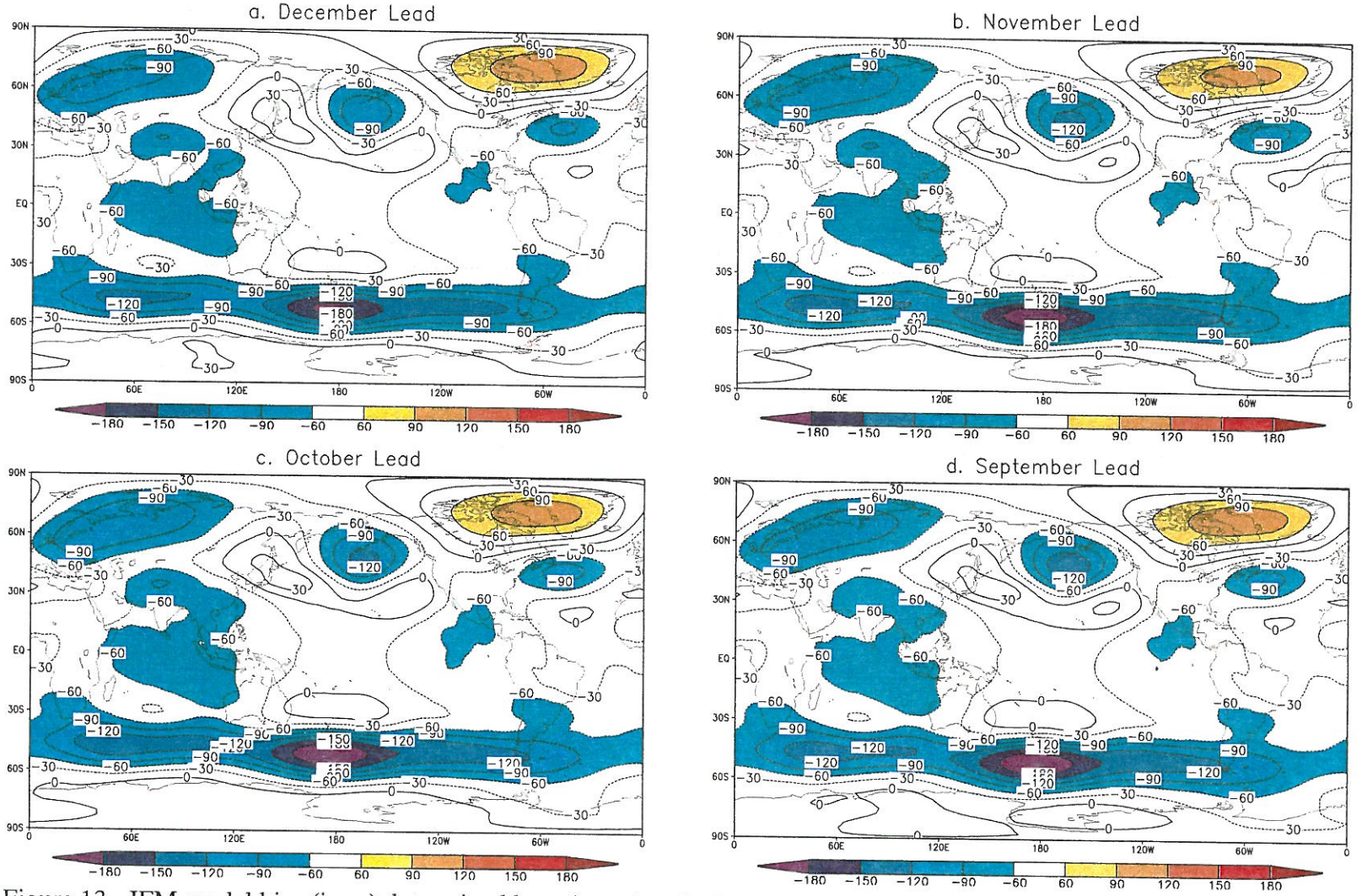

Figure 13. JFM model bias (in m) determined by subtracting the Reanalysis climatology from the model climatology for the a) December initialization, b) November initialization, c) October initialization, and d) September initialization. Contour interval is 30 m, with values greater than 60 m shaded yellow and red and values less than -60 m shaded blue and purple.

Hemisphere is now comparable to that in the Southern Hemisphere. Variability in the tropics within ~30° of the Equator is still very small and the maximum IV is still found over the North Atlantic. This is valid for all lead times.

The EV for the seasonal means (Fig. 15) reveals the same four main features shown for JAN. These are a) the dual-lobe pattern in the eastern tropical Pacific, b) the local maximum in the South Pacific, c) another local maximum over Southeast Asia, which extends across to India for JFM, and d) the dominant maximum in the North Pacific in the area of a PNA center. Overall, EV is slightly reduced compared to JAN, but not as much so as the IV detailed above. The patterns in the EV are fairly consistent, regardless of lead time.

As seen in JAN, the SNR for JFM (Fig. 16) shows a maximum for all lead times in the eastern tropical Pacific. The area where the tropical signal exceeds the noise (SNR>1) is more expansive for JFM, extending out to ~30° from the Equator. Two regions where local maxima in EV were noted also exhibit SNR>1. These are the location of the largest negative bias in the South Pacific, where SNR>1, and the area over China and India, where SNR>2. An increase in SNR over the PNA region is also noted, with SNR>1 over portions of the continental United States and SNR>2 in the North Pacific. On the whole, SNR for JFM is more consistent for varying lead times than SNR for JAN.

Anomaly correlations for JFM (Fig. 17) for the period 1980-2000 are stronger than for JAN, especially in the tropics where AC>0.8, and generally larger than 0.9, within 15° of the Equator with only a few exceptions. The area of largest AC is not confined to the eastern tropical Pacific as is found in JAN. Correlations increase to

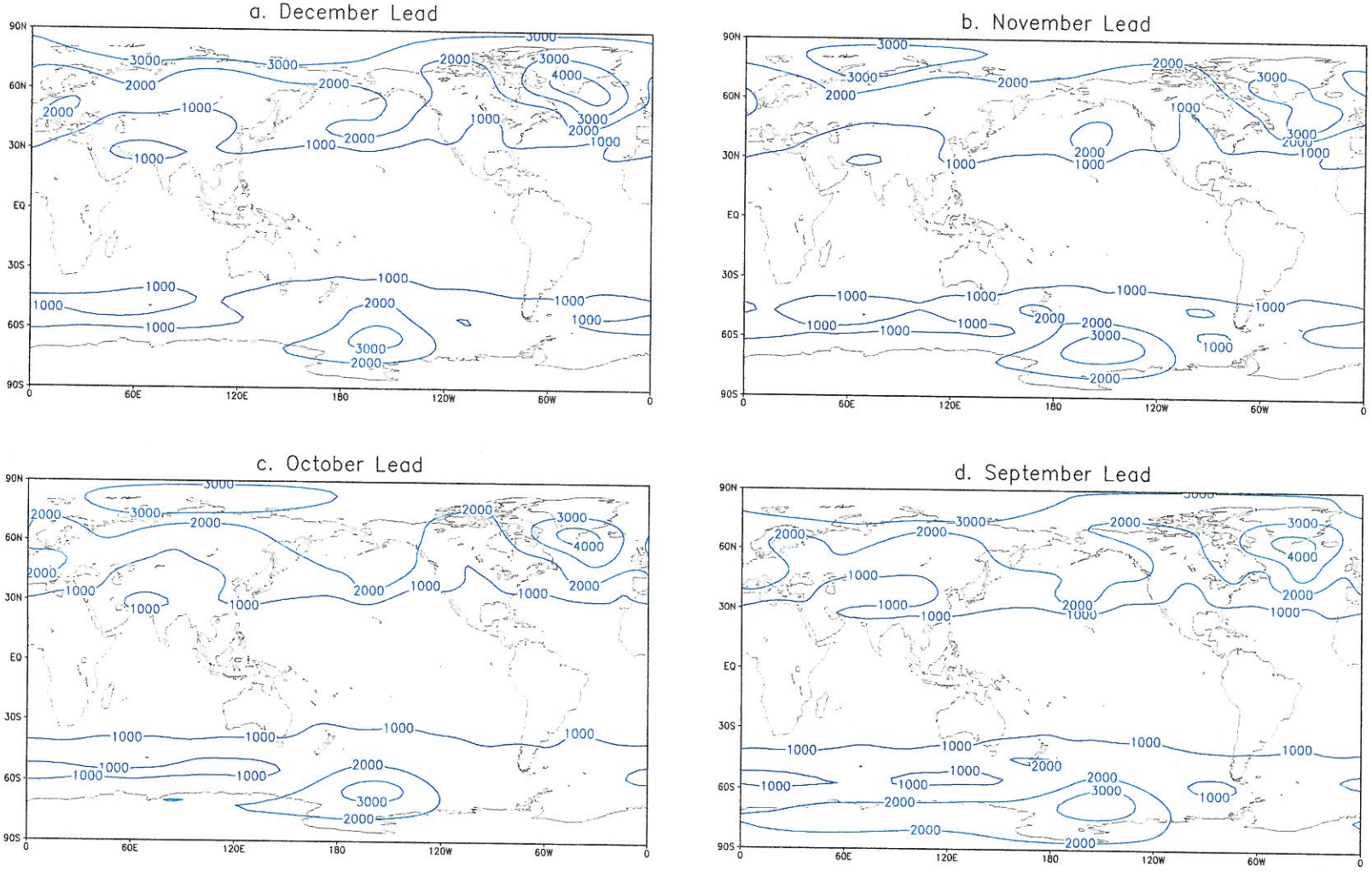

Figure 14. JFM mean internal variance (in m^2) for the a) December initialization, b) November initialization, c) October initialization, and d) September initialization. This shows the 21-year average of the variability among the 10 ensemble members in each year. Contour interval is 1000 m^2.

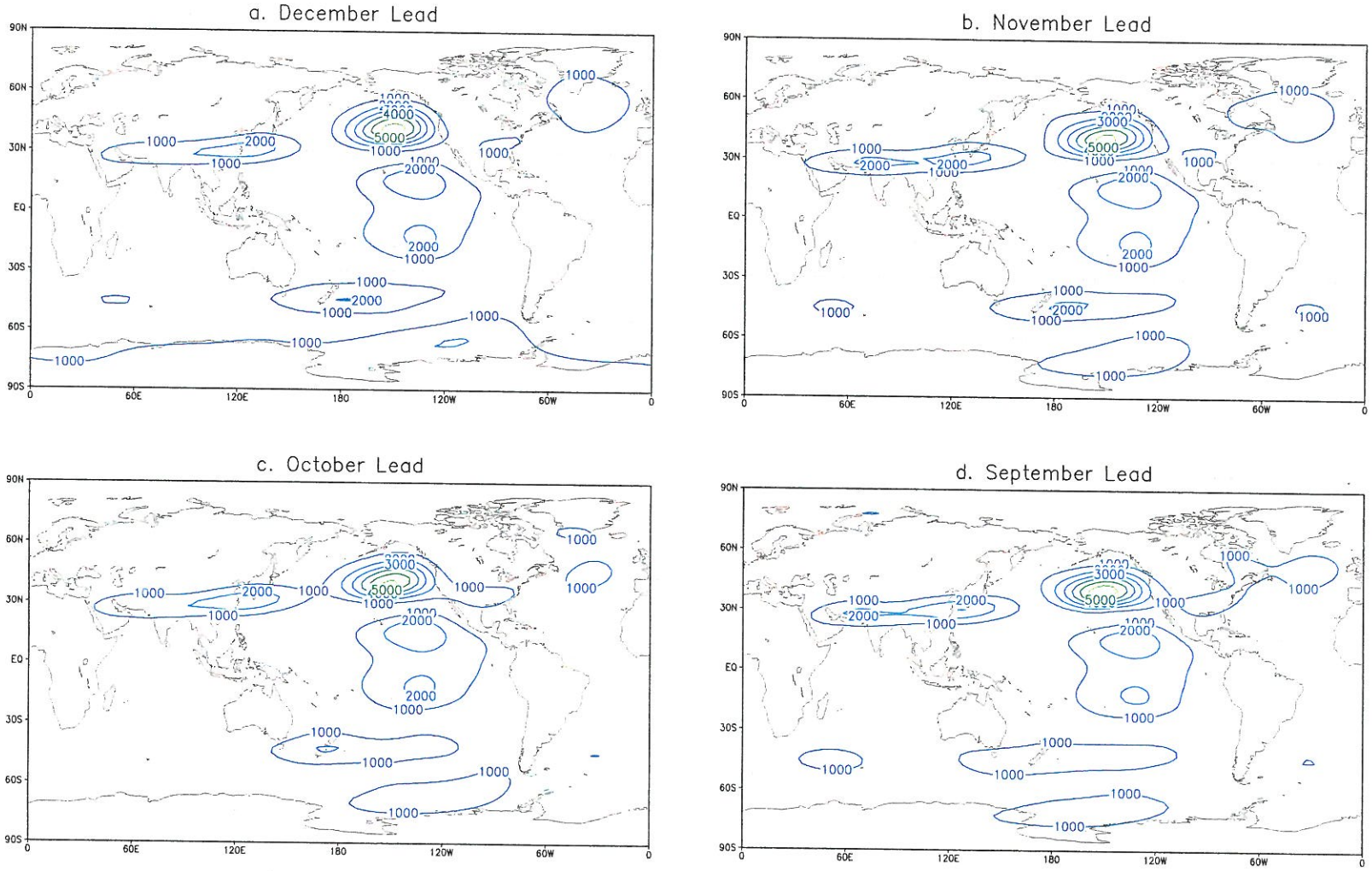

Figure 15. JFM external variance (in m^2) for the a) December initialization, b) November initialization, c) October initialization, and d) September initialization. This shows the variability among the ensemble-averaged anomalies over 21 years due only to interannual changes in SST. Contour interval is 1000 m^2.

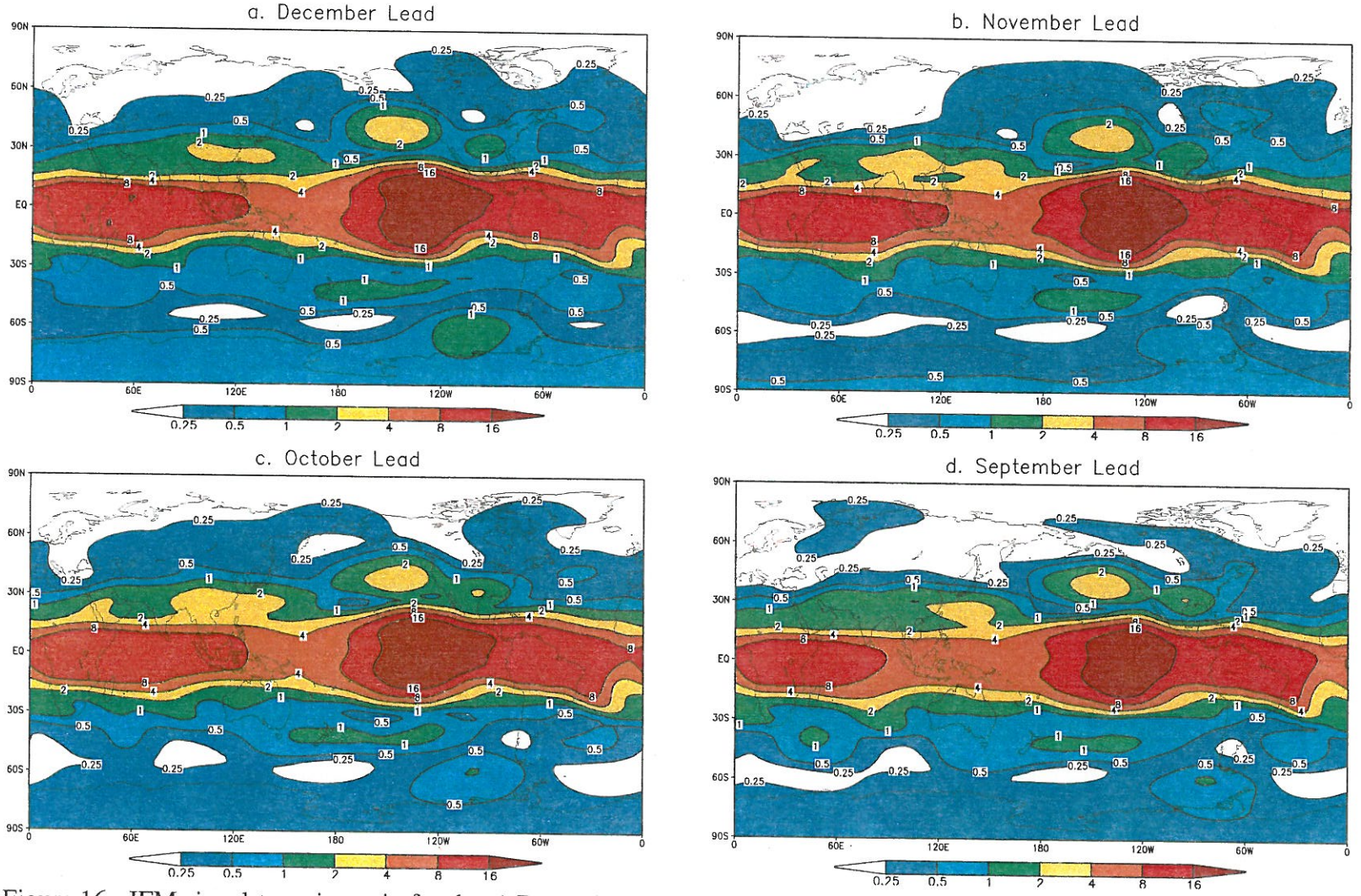

Figure 16. JFM signal-to-noise ratio for the a) December initialization, b) November initialization, c) October initialization, and d) September initialization. This is the ratio of external variance to mean internal variance. Contours for 0.25, 0.5, 1, 2, 4, 8, and 16 are shown.

beyond 0.7 for the Southern Ocean, the South Pacific, and over China and India. In the PNA region, the AC is greater than 0.8 and the area of AC>0.5 is larger, as well. Correlations over the US exceed 0.6 in some instances, a feature not seen in JAN. This pattern of AC is persistent with decreasing lead time.

Isolating the ENSO warm and cold years (Fig. 18) reveals AC of greater than 0.9 for the entire tropical belt within 20-25° of the Equator. The areal coverage of AC>0.3 is much larger, as well, when compared to all 21 years. Correlations over the Southern Ocean, the South Pacific, and over China and India increase to greater than 0.8, with isolated AC>0.9. Correlations in the PNA region exceeds 0.9 in the North Pacific and much more of the North American continent is covered by AC>0.6 when just ENSO warm and cold years are considered. As seen before, the AC pattern for ENSO warm and cold years shows little change as lead time decreases.

Anomaly correlations for ENSO neutral years for JFM (Fig. 19) are reduced when compared to AC for 1980-2000. Correlations in the tropics still exceed 0.7, which is quite skillful, but areas of AC>0.9 are nearly non-existent. The largest reduction is seen over China and India and the continental United States, where correlations drop below 0.3. Correlations over the Southern Ocean and the South Pacific still exceed 0.5, but the areal coverage of such correlations is quite small. The largest extratropical AC are still found in the PNA region in the North Pacific. This pattern, too, shows little variation with decreasing lead time.

Warm ENSO event composites for JFM (Fig. 20) reveal in the Reanalysis (Fig. 20a) a pattern somewhat similar to JAN, with a negative center in the North Pacific, south of Alaska. Moderate negative anomalies extend eastward from this center across the

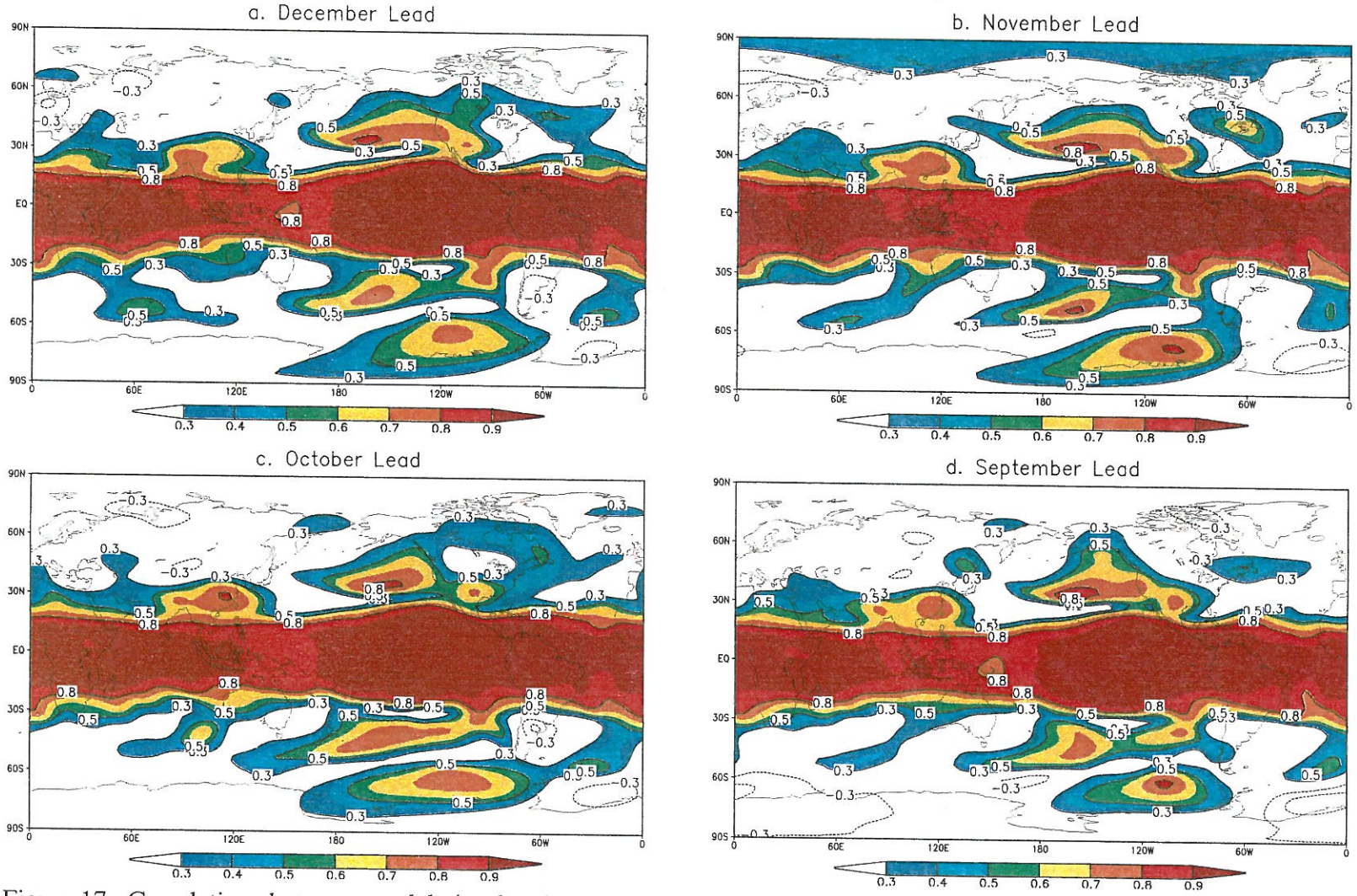

Figure 17. Correlations between model-simulated ensemble-averaged height anomalies and Reanalysis anomalies at 200 hPa for seasonal mean JFM for the a) December initialization, b) November initialization, c) October initialization, and d) September initialization. Contour interval is 0.1 for absolute values greater than 0.3. Positive (negative) contours are solid (dashed).

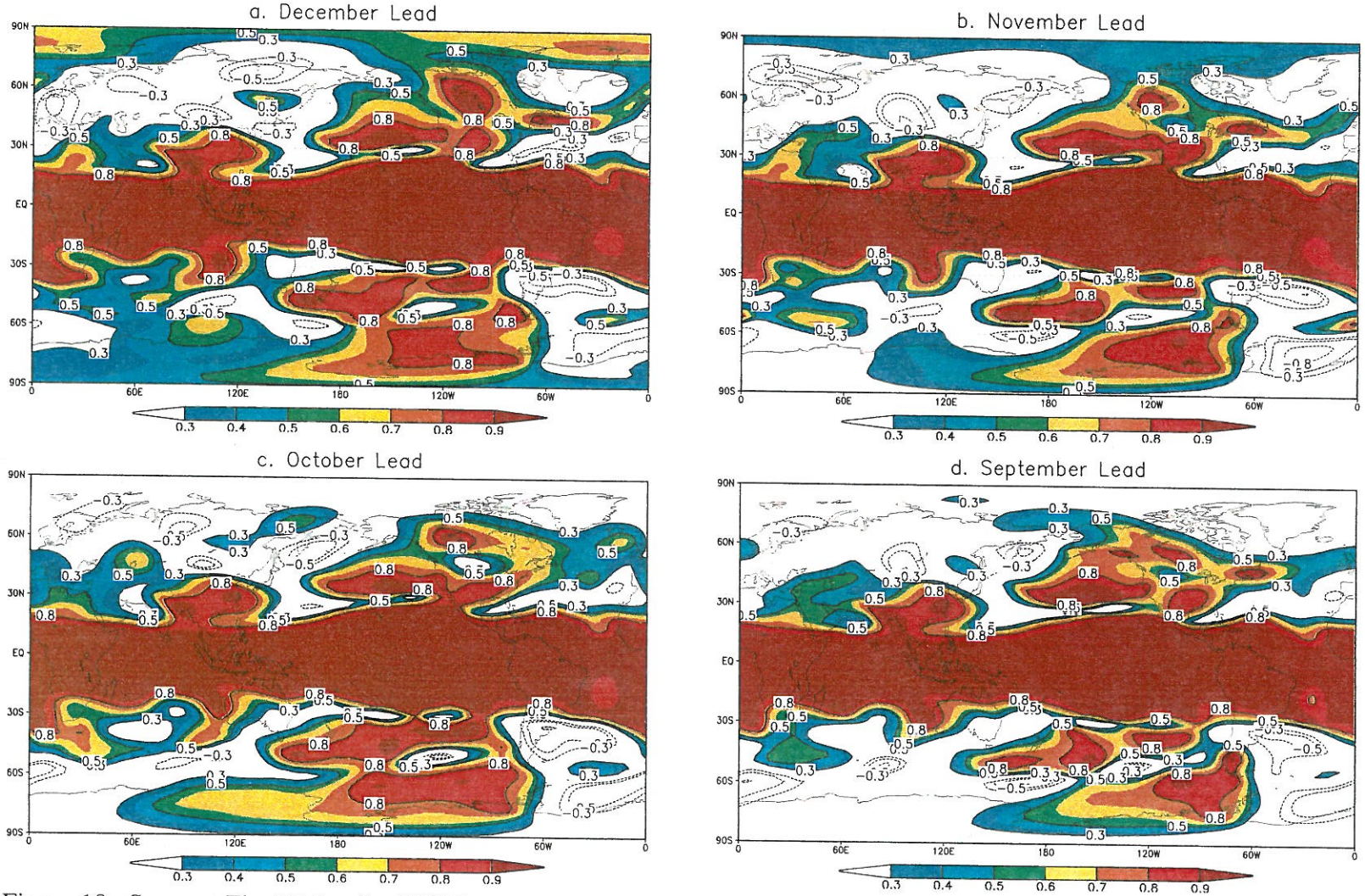

Figure 18. Same as Fig. 17, but for ENSO warm and cold events according to Table 2.

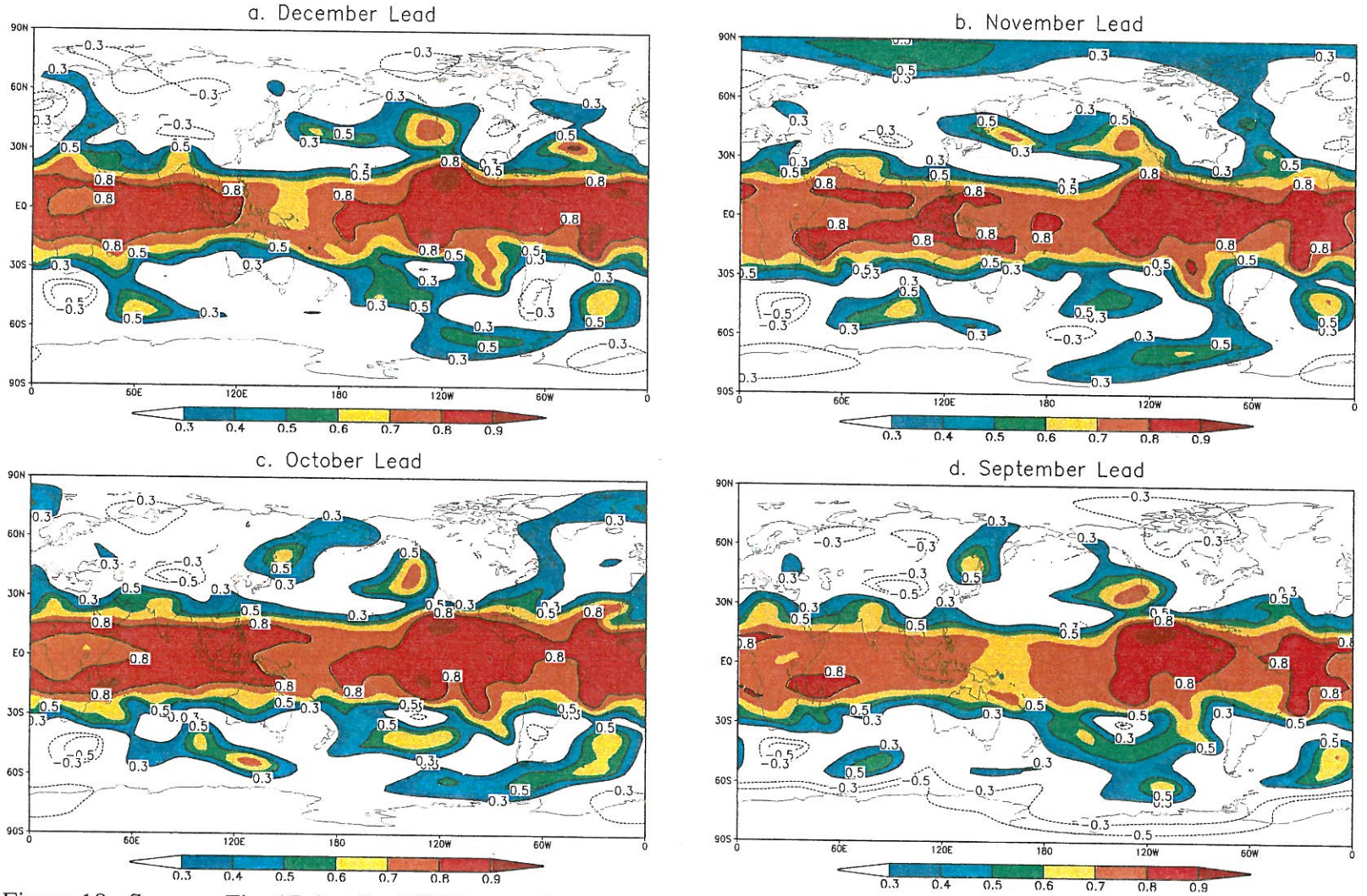

Figure 19. Same as Fig. 17, but for ENSO neutral events according to Table 2.

southern United States, but no secondary negative center is present. A strong positive anomaly is located over Hudson Bay with a magnitude slightly reduced compared to JAN. Model composites (Figs. 20b, 20d, 20f, and 20h) reveal a positive center in the North Pacific of similar magnitude but that has been shifted eastward compared to the Reanalysis. The model composites show a secondary negative center over the southern United States embedded in the eastward extension that is slightly stronger than the Reanalysis composite. The major difference is the positive anomaly center. The model response is only about one-quarter that of the Reanalysis, though the position is consistent. Differences between model composites and the Reanalysis composite (Figs. 20c, 20e, 20g, and 20i) show very little change as lead time decreases.

JFM cold ENSO composites (Fig. 21), as seen with JAN, are not exact opposites to their warm counterparts. For the Reanalysis composite (Fig. 21a), positive anomalies are found over the North Pacific and the continental United States, while a negative anomaly is centered over Alaska. The pattern for JFM is not as extreme as the cold composite for JAN, especially concerning the negative anomaly over Alaska. In the model composites (Figs. 21b, 21d, 21f, and 21h), the positive center over the North Pacific is in the same location as the Reanalysis, but of greater magnitude. The negative center over Alaska and the secondary positive center over the United States collocate well with similar magnitudes compared to the Reanalysis anomalies. Again, differences between model composites and the Reanalysis composite (Figs. 21c, 21e, 21g, and 21i) are very consistent. Overall, the best match among the four comparisons is for JFM cold events, with only the magnitude of the primary positive center drastically different between the model output and Reanalysis.

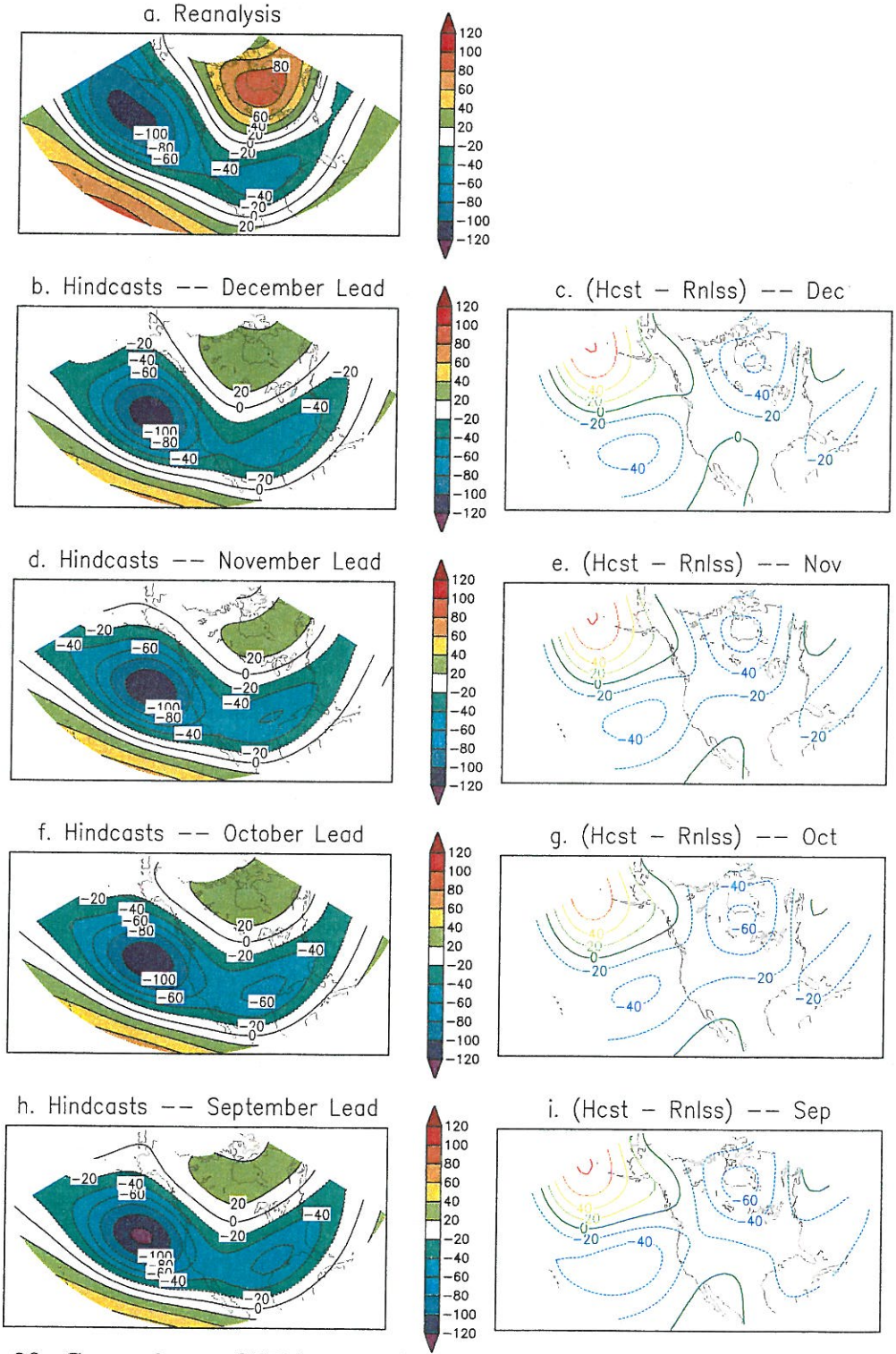

Figure 20. Comparisons of JFM composite ENSO warm event anomalies over the PNA region: a) Reanalysis, b) December initialization, c) difference (b-a), d) November initialization, e) difference (d-a), f) October initialization, g) difference (f-a), h) September initialization, and i) difference (h-a). Contour interval is 20 m.

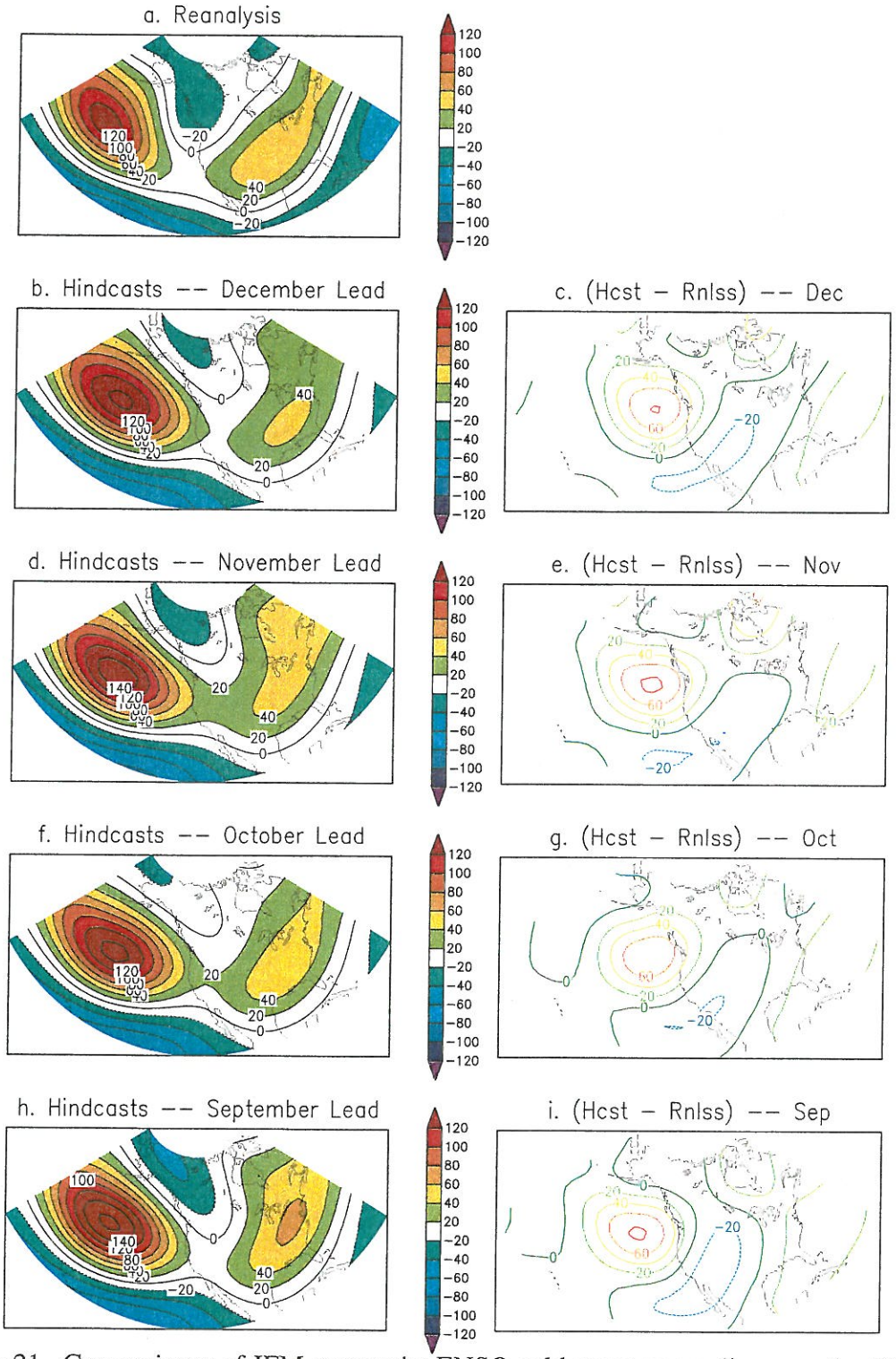

Figure 21. Comparisons of JFM composite ENSO cold event anomalies over the PNA region: a) Reanalysis, b) December initialization, c) difference (b-a), d) November initialization, e) difference (d-a), f) October initialization, g) difference (f-a), h) September initialization, and i) difference (h-a). Contour interval is 20 m.

c. Eddy Height Anomalies

The same analyses were performed on monthly mean JAN and seasonal mean JFM eddy HA (not shown). Eddy HA were formed by removing the zonal mean anomaly from the standard height anomalies that were described earlier. Results, in general, were less satisfactory for the eddy height anomalies when compared to the height anomalies. For monthly mean JAN, ACs greater than 0.3 were less expansive and areas with significant correlations (0.8 or higher) were confined to only the equatorial Pacific basin. For seasonal mean JFM, a similar reduction in the areal coverage of AC was found, though significant correlations did consistently expand into southeast Asia and the Maritime Continent for each lead time. Signal-to-noise ratios for eddy HA revealed no new regions where signal routinely exceeded noise.

5. DISCUSSION

Hindcasted 200-hPa geopotential heights from the second generation NCEP Dynamical Seasonal Forecast System are used to assess the potential predictability and skill of model-simulated wintertime monthly JAN and seasonal JFM means. In particular, the role of atmospheric initial conditions is investigated by comparing model output from lead times varying from one month up to four months. As demonstrated earlier, no significant changes are noted for any of the parameters in this study as lead time decreased for both monthly and seasonal means. Patterns in model biases, anomaly correlations, and signal-to-noise ratios are consistent for each initialization time. This suggests that, for lead times of one month or more, atmospheric initial conditions have very little influence on the monthly or seasonal mean variability of upper level atmospheric circulation during boreal winter. This is not to say that atmospheric initial conditions are completely unimportant, just that their effects are minimal for lead times of one month or more. Operational constraints at NCEP/CPC require a minimum lead time of one month. NCEP/CPC products are released to the public on the Thursday closest to the middle of the month. Thus, to allow adequate time for data processing and analysis, this one-month lead is the shortest possible lead time. Perhaps lead times of less than a month may show more influence from atmospheric initial conditions.

Based primarily on a marked increase in signal-to-noise ratio, predictions on seasonal time scales may be more reliable than monthly forecasts. External variability of

ensemble-averaged anomalies is larger for monthly means compared to seasonal means. That is, the predictable signal is slightly reduced for the seasonal means. However, an effect of the time averaging to produce the seasonal mean is that the mean internal variance is reduced by approximately one-third. This reduction in the unpredictable noise is greater than the decrease in predictable signal. It is argued that this reduction in noise is the primary cause of the increased predictability of seasonal means.

Results from correlations between hindcasted ensemble-averaged anomalies and Reanalysis anomalies suggest that the model simulates the changes associated with ENSO warm and cold events quite well. The model more accurately simulates upper-air conditions for ENSO warm and cold events than for the period 1980-2000 or the subset of ENSO neutral events. The improvement for ENSO warm and cold events compared to ENSO neutral events is considerable. Comparisons of composite events for the PNA region suggest that cold events may be simulated slightly better than warm events. However, with such a small sample of warm and cold events, no strong conclusions can be made with regard to this secondary suggestion. These composites also reveal a PNA-type response during ENSO warm events and a somewhat reverse PNA response during ENSO cold events. Neither of these findings are totally unexpected. The fact that extreme ENSO warm and cold events are simulated more skillfully than neutral events, though, is undeniable. The skill exhibited in hindcasting monthly and seasonal means using observed SSTA to force the model also suggests that accurate forecasts of forcing fields in a coupled system should yield positive results for climate forecasts, especially for the extreme events associated with ENSO.

The most encouraging result is the identification of areas outside of the tropics and the PNA region where the model skillfully simulated the atmosphere. The tropical atmosphere is generally assumed to be directly driven by fluctuations in SSTA in the tropical Pacific Ocean. Thus, the high correlations and signal-to-noise ratios in the global tropics are not surprising. It has also been shown that effects of the interannual changes in SSTA in the tropical Pacific are teleconnected to the PNA region, such that the level of skill displayed there in the model simulations was also expected. However, the skill exhibited in the South Pacific, the Southern Ocean, and in Southeast Asia was not anticipated. Ideally, it is hoped that these areas of skill could be expanded to provide a more global coverage. The identification of additional areas where the model skillfully replicates the atmosphere, especially in the extratropics away from the primary forcing mechanism, provides more confidence in the forecasting of monthly and seasonal atmospheric anomalies.

ACKNOWLEDGMENTS

Funding for this project was provided in the form of a NOAA/NCEP/FSU Fellowship in conjunction with the COAPS/Applied Research Center and the NCEP/Climate Prediction Center. COAPS receives its base funding from the NOAA Office of Global Programs.

First, I'd like to thank Dr. James J. O'Brien, for providing me with the chance to come to Florida State. My only regret is that I did not take advantage of the use of his pond on a more regular basis. Next, thanks goes to Dr. Arun Kumar at NCEP/CPC for providing me with the data used in this project. His guidance and expertise on the topic throughout the project is greatly appreciated. Also at NCEP/CPC is Dr. Jae Schemm. Her help with various computer programming problems while at NCEP is also appreciated.

Manuscript reviews by Dr. Debbie Hanley and Dr. Tim LaRow were of great help and very much appreciated. Josh Grant provided a short program for correctly placing the captions on the figures. This program saved me lots of headache and time and is also greatly appreciated. Finally, I can't go without mentioning the wide array of people I have met in the past two years at COAPS. I had never been around such a diverse group of people in my life and I truly enjoyed the great experience here at COAPS.

REFERENCES

Blackmon, M. L., J. E. Geisler, and E. J. Pitcher, 1983: A general circulation model study of January climate anomaly patterns associated with interannual variation of equatorial Pacific sea surface temperatures. *J. Atmos. Sci.*, **40**, 1410-1425.

Brankovic, C., T. N. Palmer, and L. Ferranti, 1994: Predictability of seasonal atmospheric variations. *J. Climate*, **7**, 217-237.

Chervin, R. M., 1986: Interannual variability and seasonal climate predictability. *J. Atmos. Sci.*, **43**, 233-251.

Chou, M.-D. and M. J. Suarez, 1994: An efficient thermal infrared radiation parameterization for use in general circulation models. Technical report on Global Modeling and Data Assimilation, National Aeronautical and Space Administration/TM-1994-104606, 3, 85 pp.

Dorman, J. L. and P. J. Sellers, 1989: A global climatology of albedo, roughness, and stomatal resistance for atmospheric general circulation models as represented by the Simple Biosphere Model (SiB). *J. Appl. Meteor.*, **28**, 833-855.

Geisler, J. E., M. L. Blackmon, G. T. Bates, and S. Muñoz, 1985: Sensitivity of January climate response to the magnitude and position of equatorial Pacific sea surface temperature anomalies. *J. Atmos. Sci.*, **42**, 1037-1049.

Hoerling, M., A. Kumar, and M. Zhong, 1997: El Niño, La Niña, and the nonlinearities of their teleconnections. *J. Climate*, **10**, 1769-1786.

Horel, J. D. and J. M. Wallace, 1981: Planetary-scale atmospheric phenomena associated with the Southern Oscillation. *Mon. Wea. Rev.*, **109**, 813-829.

Ji, M., A. Leetma, and J. Derber, 1995: An ocean analysis system for seasonal to interannual climate studies. *Mon. Wea. Rev.*, **123**, 460-481.

Kanamitsu, M., 1989: Description of NMC global data assimilation and forecast system. *Wea. Forecasting*, **4**, 335-342.

Kanamitsu, M., W. Ebisuzaki, J. Woollen, S.-K. Yang, J. Hnilo, M. Fiorino and G. Potter, 2002a: NCEP/DOE AMIP-II Reanalysis (R-2). Submitted to *Bull. Amer. Meteor. Soc.*

Kanamitsu, M., A. Kumar, H.-M. H. Juang, J.-K. Schemm, W. Wang, F. Yang, S.-Y. Hong, P. Peng, W. Chen, and M. Ji, 2002b: NCEP dynamical seasonal forecast system 2000. Submitted to *Bull. Amer. Meteor. Soc.*

Kistler, R., E. Kalnay, W. Collins, S. Saha, G. White, J. Woollen, M. Chelliah, W. Ebisuzaki, M. Kanamitsu, V. Kousky, H. van den Dool, R. Jenne, and M. Fiorino, 2001: The NCEP-NCAR 50-year reanalysis: monthly means CD-ROM and documentation. *Bull. Amer. Meteor. Soc.*, **82**, 247-267.

Kumar, A. and M. Hoerling, 1995: Prospects and limitations of seasonal atmospheric GCM predictions. *Bull. Amer. Meteor. Soc.*, **76**, 335-345.

Kumar, A. and M. Hoerling, 1997: Interpretation and implications of the observed inter-El Niño variability. *J. Climate*, **10**, 83-91.

Kumar, A. and M. Hoerling, 1998: Annual cycle of Pacific-North American seasonal predictability associated with different phases of ENSO. *J. Climate*, **11**, 3295-3308.

Kumar, A., M. Hoerling, M. Ji, A. Leetmaa, and P. Sardeshmukh, 1996: Assessing a GCM's suitability for making seasonal predictions. *J. Climate*, **9**, 115-129.

Lau, N.-C., 1985: Modeling the seasonal dependence of the atmospheric response to observed El Niños in 1962-76. *Mon. Wea. Rev.*, **113**, 1970-1996.

Madden, R. A., 1976: Estimates of the natural variability of time-averaged sea-level pressure. *Mon. Wea. Rev.*, **104**, 942-952.

Moorthi, S. and M. J. Suarez, 1992: Relaxed Arakawa-Schubert: A parameterization of moist convection for general circulation models. *Mon. Wea. Rev.*, **120**, 978-1002.

Pacanowski, R. C. and S.G.H. Philander, 1981: Parameterization of vertical mixing in numerical models of tropical oceans. *J. Phys. Oceanogr.*, **11**, 1443–1451.

Pan, H.-L. and W.-S. Wu, 1995: Implementing a mass flux convection par package for the NMC medium-range forecast model. NMC Office Note, No. 409, 40 pp.

Pan, H.-L. and L. Mahrt, 1987: Interaction between soil hydrology and boundary layer developments. *Bound.-Layer Meteor.*, **38**, 185-202.

Salapata, D. J., 2002: Wintertime temperature and precipitation verification of the NCEP operational climate prediction model. M.S. Thesis, Department of Meteorology, The Florida State University, 52 pp. [Available from Center of Ocean-Atmospheric Prediction Studies, The Florida State University, Tallahassee, FL 32306-2840.]

Shukla, J., 1983: Comments on "Natural variability and predictability". *Mon. Wea. Rev.*, **111**, 581-585.

Shukla, J. and D. S. Gutzler, 1983: Interannual variability and predictability of 500 mb geopotential heights over the Northern Hemisphere. *Mon. Wea. Rev.*, **111**, 1273-1279.

Slingo, J. M., 1987: The development and verification of a cloud prediction model for the ECMWF model. *Quart. J. Roy. Meteor. Soc.*, **113**, 899-927.

Straus, D. M. and J. Shukla, 2000: Distinguishing between the SST-forced variability and internal variability in mid-latitudes: Analysis of observations and GCM simulations. *Quart. J. Roy. Meteor. Soc.*, **126**, 2323-2350.

Wallace, J. M. and D. S. Gutzler, 1981: Teleconnections in the geopotential height field during the Northern Hemisphere winter. *Mon. Wea. Rev.*, **129**, 784-812.

Yarnal, B. and H. F. Diaz, 1986: Relationship between extremes of the Southern Oscillation and the winter climate of the Anglo-American Pacific coast. *J. Climatol.*, **6**, 197-219.